Prompt and sequential decay processes in the fragmentation of 40 MeV/nucleon ^{20}Ne projectiles

R. J. Charity,[1] L. G. Sobotka,[1,2] N. J. Robertson,[2] and D. G. Sarantites[1]
[1]*Department of Chemistry, Washington University, St. Louis, Missouri 63130*
[2]*Department of Physics, Washington University, St. Louis, Missouri 63130*

J. Dinius, C. K. Gelbke, T. Glasmacher, D. O. Handzy, W. C. Hsi, M. J. Huang, W. G. Lynch, C. P. Montoya,* G. F. Peaslee,† C. Schwarz,‡ and M. B. Tsang
National Superconducting Cyclotron Laboratory and Department of Physics and Astronomy, Michigan State University, East Lansing, Michigan 48824
(Received 15 May 1995)

The fragmentation of $E/A = 40$ MeV ^{20}Ne projectiles into exit channels containing only p, d, t, ^{3}He, α, ^{6}He, ^{6}Li, and ^{7}Li fragments has been investigated. Relative shifts between the average longitudinal velocity of each fragment type were measured with ^{120}Sn and ^{197}Au targets. A post-breakup Coulomb acceleration component of these shifts was isolated. Its magnitude indicates that the projectile broke up while in near contact with the target. On the other hand, correlations between projectile fragments indicate that a significant fraction of these fragments are produced by the sequential decay of long- and short-lived unstable intermediates. A fully sequential decay process, although consistent with the experimental relative angle distributions, fails to reproduce the correlation function. Thus, a picture emerges of a prompt breakup step producing stable and unstable particles with the subsequent decay of the latter extending over a long time period.

PACS number(s): 25.70.Mn, 25.70.Lm

I. INTRODUCTION

The phenomenon of projectile fragmentation has been studied over a wide range of bombarding energies. The mechanisms attributed to projectile fragmentation range from direct breakup [1,2] to the excitation and sequential decay of the projectile [3,4]. Recently with the advent of large detector arrays, attention has been focused on events where the projectile disassembles into many pieces. From measurements of exit channel cross sections [5–7] it has been suggested that such channels result from the statistical decay of highly excited projectiles. Several projectile fragmentation studies [4,8,9] have also addressed the important question in intermediate energy collisions as to whether the fragmentation of hot nuclei is a prompt decay process or proceeds via a series of slower sequential decay steps [10]. The above studies compare relative angle and event shape distributions predicted by simulations of prompt and sequential decay mechanisms to experimental data. They conclude that projectile fragmentation is mainly sequential as the sequential simulations reproduce the experimental distributions while the prompt do not. However, because of the simplicity of the prompt decay simulation in the cited works, which have neglected the inevitable decay of directly populated resonances [11], this conclusion must be reexamined in the light of improved simulations and, as will be shown, more discriminating observables.

Questions concerning the sequential or direct nature of the projectile disassembly can be addressed from measurements of the time scales involved. Correlation functions are now extensively used in more central collisions to extract such information [12,13]. Another fruitful approach to measuring such time scales in peripheral collisions is to use the post-breakup accelerations, from the target's Coulomb field, as a clock. Attempts at using such a clock include looking for distortions in the emission pattern of a fragment due to the gradient of the Coulomb field [9,11,14] to measuring relative shifts in the longitudinal velocity spectra of different fragment types resulting from the Z/A dependence of the Coulomb accelerations [15,16]. Recently, we have reported measuring Coulomb shifts between alpha particles and protons produced in the disassembly of highly excited ^{24}Mg projectiles [16]. The magnitude of these shifts implies that the protons were emitted from the projectile within 3×10^{-22} s after it separated from the target. This result again raises questions as to whether previous interpretations of a sequential decay mechanism for projectile fragmentation are correct and whether a more direct decay process may be occurring.

To answer these questions and further confirm the nature of the Coulomb shifts, we have measured correlation functions and longitudinal velocity spectra for a large variety of fragment types produced by the fragmentation of $E/A = 40$ MeV ^{20}Ne projectiles. The experimental apparatus and the criteria for event selection are described in Secs. II and III. The presence of a prompt decay component is determined from the analysis of the longitudinal velocity spectra. The extraction of the Coulomb shifts is presented in Sec. IV. On the other hand, the correlation functions discussed in Sec. V show the importance of the sequential decay of long- and short-lived intermediates. The conclusions of this work are summarized in Sec. VII.

* Present address: Merrill Lynch, New York, New York.
† Present address: Physics Department, Hope College, Holland, Michigan.
‡ Present address: Gesellschaft für Schwerionenforschung, Darmstadt, Germany.

TABLE I. Number of detectors and minimum and maximum angles for each ring of the MINIWALL array. Note that detectors in a ring do not exactly follow an arc and so there is a small overlap in the angular range of adjacent rings.

Ring	Number of detectors	Minimum angle	Maximum angle
1	16	3.4	5.4
2	16	5.4	8.7
3	22	8.5	11.6
4	26	11.5	14.6
5	24	14.5	18.9
6	24	19.1	25.5

II. EXPERIMENTAL METHOD

A ^{20}Ne beam of $E/A=40$ MeV was extracted from the NSCL K1200 cyclotron and impinged on targets of ^{197}Au and ^{120}Sn. The areal densities of the targets were 3.7 and 2.9 mg/cm^2, respectively. Projectile fragments were identified in the Washington University MINIWALL array containing 128 detectors, grouped into six rings, covering the complete angular range from 3.3° to 25.5°. The number of detectors and the angular range of each ring are listed in Table I. Each detector consisted of a plastic scintillator foil of thickness 8 mg/cm^2 (with the exception of 15 mg/cm^2 for the inner ring) followed by a 3 cm thick piece of CsI. The operation of these detectors is similar to that discussed in Ref. [17].

The MINIWALL detectors have isotopic resolution for $Z\leqslant 4$ and elemental resolution for $Z\lesssim 20$. The low energy thresholds below which an isotope cannot be identified are 4 MeV and 8 MeV for hydrogen isotopes and alpha particles, respectively. The ^{3}He isotope can only be well separated from alpha particles for energies above $E/A=13$ MeV and the separation of the Li isotopes is obtained for $E/A>10$ MeV. Protons, deuterons, and tritons punch through the CsI crystals at energies above $E/A=97$, 63, and 50 MeV, respectively, and unambiguous particle identification becomes impossible.

Energy calibrations were obtained for hydrogen, helium, and lithium isotopes using fragmentation products selected from the $E/A=50$ MeV ^{7}Li + ^{27}Al reaction with the A1200 spectrometer [18]. The secondary beams obtained from this procedure are listed in Table II. The isotope dependence of the energy calibrations was almost identical for all the detectors with deviations from the average of no more than $\pm 2\%$. As the energy resolution of a detector is also $\sim 2\%$, this permitted the use of a single isotope dependence of the calibration to be assumed for all detectors.

The MINIWALL detectors were also able to separate and identify situations where two alpha particles entered the same detector ("2α fragment"). Most of these alpha particles are the decay products of the ground state of ^{8}Be. However, for a significant number of ^{8}Be fragments, such alpha particles were detected in neighboring detectors. Also, as some 2α fragments result from uncorrelated α pairs, no attempt was made to separate events with and without ^{8}Be fragments. All events were classified by the total number of detected alpha particles, but separate spectra were produced for the 2α fragments.

TABLE II. Secondary beams used for energy calibration of MINIWALL detectors.

Isotope	E/A (MeV)
^{1}H	48.6
^{2}H	12.4, 39.7
^{3}H	5.5, 43.2
^{3}He	21.9
^{4}He	12.5, 40.0
^{6}He	5.5, 43.2
^{6}Li	12.4, 39.9
^{7}Li	9.1, 50.0

Charged fragments emitted by the target were detected in the MSU MINIBALL array [19] which covered polar angles from 31° to 160°. In this publication, only the multiplicity of the charged particles detected in this device will be presented.

III. EVENT SELECTION

In order to select events which are well characterized as resulting from projectile fragmentation, criteria were imposed to restrict the velocities of the fragments. The reconstructed velocity $V_{\rm PLF}$ of the projectilelike fragment (PLF), obtained from the center of mass of the detected fragments, was required to be greater than 83% of the beam velocity. Also, the sum kinetic energy of all detected fragments in the PLF frame, $E_{\rm tot}$, was required to be less than 5.75 MeV $\times\Sigma Z$, where ΣZ is the total detected charge. Monte Carlo simulations (Appendix A) indicate that these selection criteria minimize distortions in the longitudinal velocity spectra resulting from the detector thresholds and geometry. However, the criteria also restrict the analysis to the more peripheral collisions. This is also advantageous as it reduces the probability of contamination from events where a target fragment is included with the projectile fragments.

With these selection criteria, 25 exit channels were found with reasonable yields containing only p, d, t, ^{3}He, α, ^{6}Li, ^{7}Li, and 2α fragments for which $\Sigma Z=10$. The yields of these highly fragmented events are listed in Table III for the reaction with the Au target. The yields obtained with the Sn target are generally 20–30 % higher. The charged fragment multiplicity in the selected channels ranges from 4 to 7 and the total detected nucleon number (ΣA) ranges from 16 to 22. Channels with $\Sigma A>20$ must involve the transfer of neutrons from the target. However, as neutrons were not detected, it is not clear whether channels with $\Sigma A\leqslant 20$ are associated with transfer reactions or not. The ratios of yields for the two targets, normalized to unity for the 5α channel, are also listed in the table. The relative yields for the different channels are similar, but not identical, for the two targets.

Thirty-two channels were also selected for $\Sigma Z=8$ events which involve the transfer of protons from the projectile. The yields of these channels obtained with the Au target are listed in Table IV. Monte Carlo simulations (Appendix A) suggest that only $\approx 2\%$ of the $\Sigma Z=8$ events are expected to arise from incompletely detected $\Sigma Z=9$ and 10 events. For $\Sigma Z=12$ events, only two channels were found with reasonable yields: 5α+2p (418 events) and 6α (314 events).

TABLE III. Exit channel yields obtained for $\Sigma Z=10$ events. Values obtained with the Au target are listed along with the ratio of yields obtained with the Sn and Au targets normalized to unity for the 5α channel. Estimates of the excitation energy are listed for some channels.

Channel	Events (Au)	Sn/Au	E^* (MeV)
5α	53163	1.00±0.01	45
$4\alpha+2p$	13160	1.18±0.01	96
$4\alpha+p+d$	8645	1.19±0.02	86
4α + ^{3}He	7760	1.12±0.02	79
3α + ^{7}Li+p	6583	1.09±0.02	65
3α + ^{6}Li+p	5785	1.20±0.02	84
$4\alpha+p+t$	4802	1.00±0.02	72
3α + ^{6}Li +d	2158	1.11±0.03	72
3α + ^{7}Li + d	2056	0.99±0.03	
$4\alpha+2d$	1446	1.09±0.03	77
3α + ^{3}He +$2p$	1283	1.37±0.04	130
$4\alpha+d+t$	1267	0.88±0.04	
2α + ^{6}Li + ^{7}Li	1067	1.06±0.04	
3α + ^{3}He + $p+d$	956	1.32±0.04	119
3α + ^{6}Li + t	933	0.94±0.04	
2α + 2^{6}Li	609	1.14±0.05	68
3α + ^{7}Li + t	590	0.84±0.05	
3α + ^{3}He + $p+t$	533	1.16±0.06	105
3α + 2^{3}He	492	1.29±0.06	112
$3\alpha+3p+d$	476	1.30±0.06	138
2α + 2^{7}Li	399	1.00±0.08	
$3\alpha+3p+t$	333	1.28±0.08	119
$3\alpha+4p$	310	1.44±0.10	147
3α + $2p$ + d + t	270	1.15±0.09	112
$3\alpha+2p+2d$	226	1.28±0.10	127

Typical distributions of $V_{\rm PLF}$ and $\theta_{\rm PLF}$, the PLF scattering angle, are shown in Figs. 1 and 2 for the $4\alpha+2p$ exit channel. The reconstructed velocities of the PLF extend all the way up to the value for elastic scattering. The low velocity cutoff is a result of the event selection criteria. Over all exit channels, the average value of $V_{\rm PLF}$ varies by at most 0.3 cm/ns. The angular distributions are peaked at zero degrees and they extend past the grazing angle located at ~5°. Again, the angular distributions are very similar for all

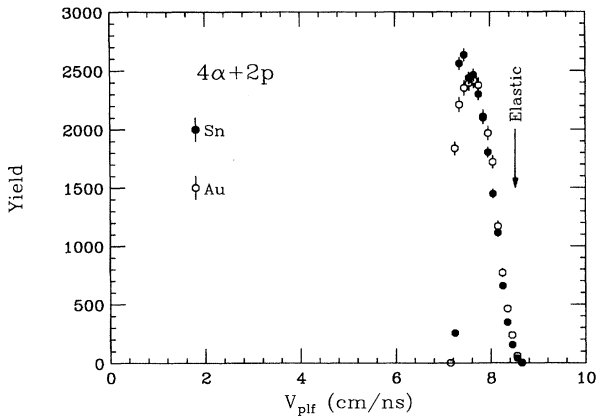

FIG. 1. Velocity distributions of reconstructed PLF's in the laboratory frame for the $4\alpha+2p$ exit channel. Solid and open points were obtained with the Sn and Au targets, respectively. The Au data have been normalized to the same total number of counts as for the Sn data. The arrow indicates the velocity associated with elastic scattering.

exit channels, with average values of $\theta_{\rm PLF}$ varying by at most 0.5°. For both $V_{\rm PLF}$ and $\theta_{\rm PLF}$, the distributions obtained with the Sn (solid points) and with the Au (open points) targets are nearly identical in for all exit channels.

The $E_{\rm tot}$ distributions for the same exit channel are displayed in Fig. 3. They are reasonably wide with average values of ~30 MeV and again are identical, within statistical errors, for the two targets. The excitation energy of the PLF can be determined from $E_{\rm tot}$ by subtracting the Q value for the breakup and adding the kinetic energy of the neutrons. Mean values for the excitation energy were estimated for exit channels where $\Sigma A\leqslant 20$ assuming no net transfer of mass and the mean proton and neutron kinetic energies are identical. They are listed in Table III and indicate that very excited PLF's are created; the maximum value corresponds to 7.5 MeV per nucleon. However, in each channel, approximately one-half of the excitation energy is associated with the Q value. The largest uncertainty associated with these excitation energies is due to the assumed number of undetected neutrons. If this number is increased by one, then the excitation energies will be increased by ~16 MeV. On the other

TABLE IV. Channel yields for $\Sigma Z=8$ events.

Channel	Events	Channel	Events	Channel	Events
4α	306732	$3\alpha+2d$	9358	$2\alpha+2p+d+t$	2485
$3\alpha+2p$	61613	2α + ^{3}He + $p+d$	8538	$2\alpha+4p$	2395
2α + ^{7}Li + p	53542	2α + ^{6}Li + t	8370	3α + ^{6}He	2318
$3\alpha+p+d$	47021	2α + ^{7}Li + t	7800	3α + 2t	2280
3α + ^{3}He	41362	α + ^{6}Li + ^{7}Li	7176	2α + ^{3}He + 2d	1922
2α + ^{6}Li + p	40650	2α + ^{3}He + $p+t$	4926	2α + $2p+2d$	1864
3α + $p+t$	29526	2α + 2^{3}He	4100	2α + ^{3}He + $d+t$	1881
2α + ^{7}Li + d	19297	α + 2^{7}Li	3557	2α + $p+2d+t$	810
2α + ^{6}Li + d	17293	α + 2^{6}Li	3307	2α + $2p+2t$	729
$3\alpha+d+t$	10141	2α + $3p+d$	3511	2α + ^{3}He + 2t	362
2α + ^{3}He + $2p$	9910	2α + $3p+t$	2523		

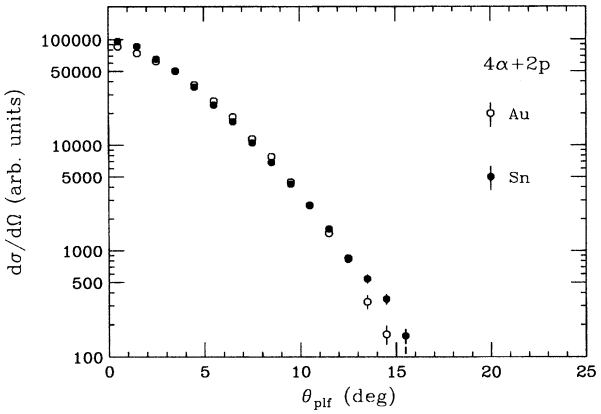

FIG. 2. Angular distributions of reconstructed PLF's in the laboratory frame for the $4\alpha+2p$ exit channel. Solid and open points were obtained with the Sn and Au targets, respectively.

hand, for one less neutron, the excitation energies will be decreased by ~ 26 MeV.

The exit channels were classified by the total number of alpha particles including both the contribution from detected α and 2α fragments. The probability that a selected event contained one or two 2α fragments is shown in Fig. 4 as a function of $E_{\rm tot}$ for the 5α exit channel. The largest probabilities occur at the smallest $E_{\rm tot}$ values (excitation energies). The one-2α probability ranges from 10% to 60% while the two-2α probability is at most 10% and becomes less than 1% for the largest $E_{\rm tot}$ values. Note, again, that the results obtained with the two targets are identical within the statistical errors. Simulations are required to deduce the ^{8}Be(g.s.) probabilities from these results. The solid and dashed curves show the ^{8}Be(g.s.) probabilities obtained from the simulations described in Appendix A and in Sec. V, respectively. In the former no interactions between the alpha particles are assumed, while Coulomb interactions are considered in the latter. For the 5α exit channel, the probability

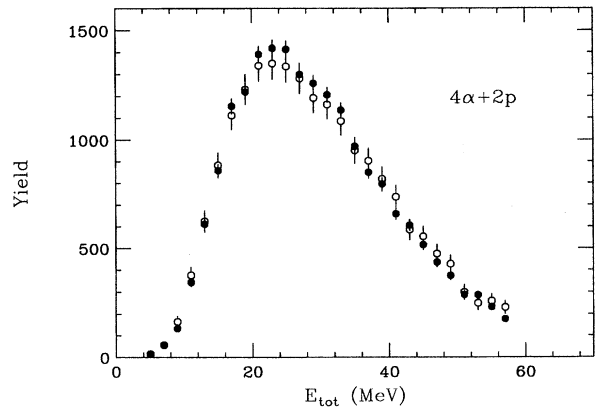

FIG. 3. Distribution of the total kinetic energy of the projectile fragments in their center-of-mass frame for the $4\alpha+2p$ exit channel. The solid and open points were obtained with the Sn and Au targets, respectively. The Au data have been normalized to the same total number of counts as for the Sn data.

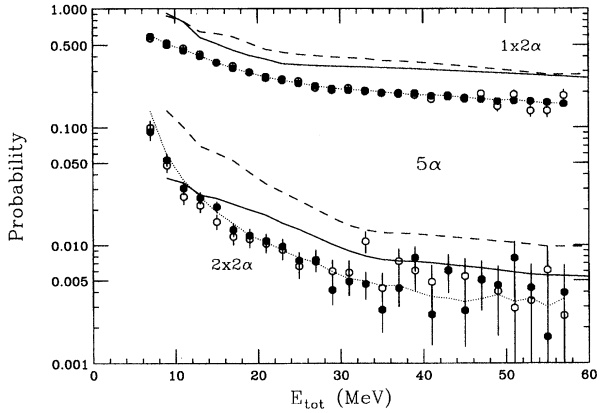

FIG. 4. Experimental probability of observing one and two 2α particles per 5α event as a function of the total kinetic energy of all projectile fragments. The open and solid data points are obtained using the Au and Sn targets, respectively. The solid curves indicate the probabilities of one and two ^{8}Be(g.s.) fragments which were included in the simulations to fit the experimental data. The fits are indicated by the dotted curves. The dashed curves indicate the ^{8}Be fragment probabilities required when Coulomb interactions between the alpha particles are also considered.

(averaged over $E_{\rm tot}$) for one and two ^{8}Be(g.s.) fragments is 45% and 2%, respectively, without interactions and 50% and 5%, respectively, with interactions. For the other exit channels these probabilities are smaller.

To confirm the peripheral nature of these events, the multiplicity $M_{\rm ball}$ of charged particle detected in the MINIBALL array ($\theta_{\rm lab}>31°$) was examined. These particles must originate from the target nucleus, if all the projectile fragments are detected in the MINIWALL array. Figure 5 shows a typical multiplicity distribution obtained for the $4\alpha+2p$ exit channel with the Au target (open points). Only very small MINIBALL multiplicities are observed in coincidence with the selected projectile fragmentation events. In contrast, the multiplicity distribution associated with all recorded events is indicated by the solid points. The experimental trigger for recording events was a multiplicity of 2, or larger, in the MINIWALL. This multiplicity distribution extends out to much larger values and, hence, the low multiplicities associated with the selected events indicate that they result from more peripheral collisions.

The MINIBALL multiplicity is also correlated with the reconstructed PLF excitation energy. This is illustrated in Fig. 6 in which the average excitation energy reconstructed for $\Sigma Z=10$ channels is plotted against the associated mean MINIBALL multiplicity. Thus, on average, larger PLF excitation energies are obtained in more dissipative collisions, presumably with somewhat smaller impact parameters.

The dependence of the MINIBALL multiplicity on ΣZ is shown in Fig. 7. For ΣZ greater than, or equal to, the projectile value, the multiplicity is rather constant. However, it increases rapidly for smaller values of ΣZ, suggesting that these transfer channels are associated with smaller impact parameters. The larger MINIBALL multiplicities for the lower ΣZ values raises the possibility of contaminated events in which a target particle, detected in the MINI-

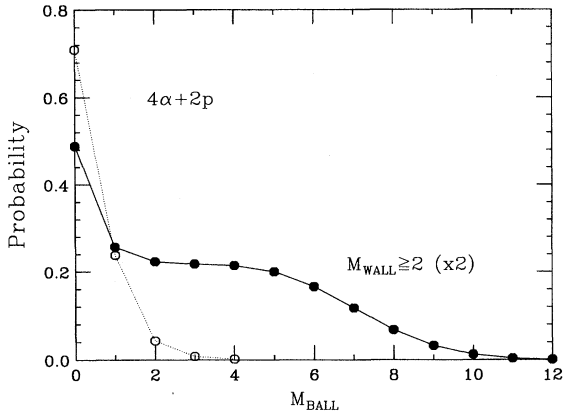

FIG. 5. Multiplicity probability distributions of particles detected in the MINIBALL array for the $4\alpha+2p$ exit channel (open points) and for all events with a multiplicity of 2, or larger, in the MINIWALL array (solid points). These results were obtained with the Au target.

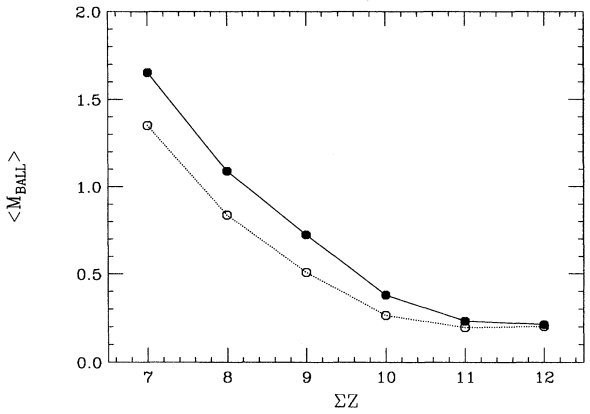

FIG. 7. The average multiplicity of particles detected in the MINIBALL array for the selected projectile fragmentation events as a function of the total Z of the projectile fragments. Solid and open data points were obtained with the Sn and Au targets, respectively.

WALL, is counted as a projectile fragment. In fact, a small "bump" ($\sim$4% yield) is observed at small longitudinal velocities in the spectra for protons for the selected $\Sigma Z=8$ events. These protons have the appropriate laboratory energy for target protons. No such structure was observed for the other particle types. This is not surprising as protons are emitted from the target with the largest velocities and hence are more likely to be confused with a projectile fragment. The proton spectra for these $\Sigma Z=8$ events will not be used in the Coulomb shift analysis. For $\Sigma Z=10,12$ channels, no "bump" feature was observed in the proton spectra.

IV. COULOMB SHIFT ANALYSIS

The longitudinal velocity (V_z) of a particle was determined event by event, relative to the center of mass of all the detected projectile fragments in the event. Spectra were constructed for each particle type and each exit channel. As an example, the spectra measured for four $\Sigma Z=10$ exit channels are plotted in Fig. 8. The results obtained with the Sn and Au targets are indicated by the solid and dashed lines, respectively. An examination of the spectra shapes shows that their low velocity tail is longer than their their high velocity tail. Although this difference is not large, it indicates that not all projectile fragments are emitted from a completely equilibrated system. As the alpha particles make up most of the mass for these channels, they essentially define the center of mass. Hence, their spectra are centered near $V_z=0$. Relative to this, the spectra for protons and ^{3}He fragments, which have larger Z/A ratios, are shifted to higher velocities, while those for tritons, which have a lower Z/A ratio, are shifted down in velocity. Surprisingly, the deuterons which have the same Z/A ratio as alpha particles are also shifted down in velocity.

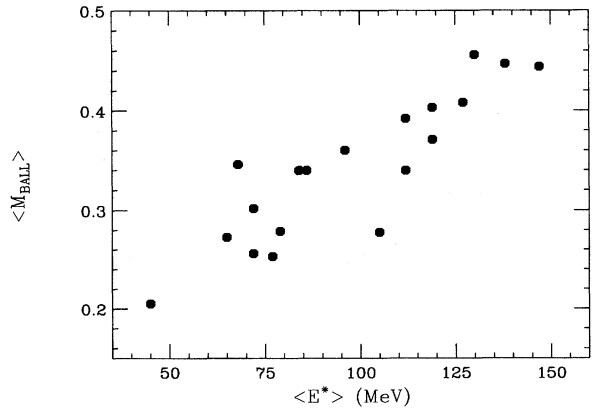

FIG. 6. Correlation between the average reconstructed excitation energy of an exit channel and the average multiplicity of fragments detected in the MINIBALL array. These results were obtained with the Au target.

Although the spectra for the two targets are very similar for all three particles, close inspection reveals small velocity shifts between them. For protons and ^{3}He fragments the centroids are shifted further up for the Au target, while those for tritons are shifted further down. On the other hand, deuterons and 2α fragments show little dependence on the target. These trends are representative of those observed for other channels and follow the expectation for post-breakup Coulomb acceleration effects. However, it will be shown that this effect cannot fully explain the absolute shifts for all particle types.

Relative to alpha particles, the average increase in the energy per nucleon of a fragment due to Coulomb accelerations is

$$\Delta(E/A)=\Delta(Z/A)\frac{Z_t e^2}{R}. \quad (1)$$

Here R is the separation between the centers of the target and the projectile when the projectile disassembles, Z_t is the target charge, and $\Delta(Z/A)$ is the difference of the fragment's Z/A value from the value of 0.5 for alpha particles. As a starting point, all detected particles will be assumed to have

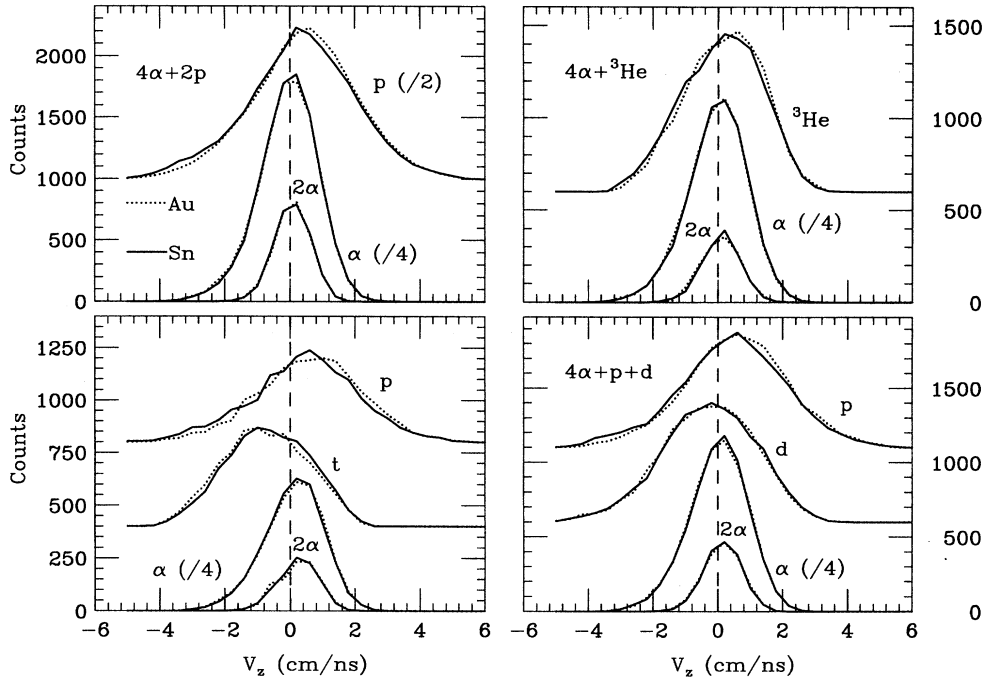

FIG. 8. Comparison of longitudinal velocity spectra of fragments from four $\Sigma Z=10$ exit channels measured with the Sn (solid curve) and the Au (dashed curve) target. For clarity, the spectra have been shifted vertically and scaled as indicated in the parentheses.

been created at the same value of R. The consequences of a sequential decay component will be examined in the subsequent sections.

A. Total shifts

Values of $\Delta(E/A)$ were calculated from the centroids of the longitudinal velocity spectra $\langle V_z \rangle$, the average projectile-target relative velocity $\langle V_{\rm rel} \rangle$, and the fragment mass m by [16]

$$\Delta(E/A)=(\langle V_z \rangle - \langle V_z \rangle_\alpha)\langle V_{\rm rel} \rangle \frac{m}{A}. \quad (2)$$

The shifts for each particle type were identical, within error, for all exit channels. The average values of these shifts for $\Sigma Z=10$ events are plotted against $\Delta(Z/A)$ in Figs. 9(a) and 9(b) for the two targets. The Monte Carlo simulations of Appendix A were used to determine correction factors to account for shifts induced by the detector bias. They were found to be negligible, except for p, t, and ^{3}He fragments. The corrected and uncorrected shifts are indicated in Fig. 9 by the solid and open points, respectively. The error bars represent the systematic errors which arise from the uncertainty in the relative energy calibrations of the fragments and from the uncertainty in the detector-bias correction. For comparison, predicted Coulomb shifts for a breakup separation of $R=14.4$ fm are indicated by the solid lines. These predictions account for the magnitudes of the proton and ^{3}He shifts. However, unphysical breakup separations (≈ 3 fm), less than the radius of the target, would be required to reproduce the magnitude of the triton shift. In addition for d, α, ^{6}Li, and 2α fragments for which $\Delta(Z/A)=0$, there is a large range of shifts which cannot be accounted for by Coulomb accelerations. Clearly some other process is contributing to these measured shifts.

B. Coulomb shifts

If the other contributions to the shifts are identical for both targets, then the Coulomb contribution can be isolated by subtracting the shifts measured with the two targets. The resulting differences should then correspond to Coulomb shifts from a target of $Z_t=Z_{\rm Au}-Z_{\rm Sn}=29$. Given the nearly identical properties of the PLF's shown in Sec. III, the above assumption is not unreasonable.

The differences in the shifts are shown in Fig. 9(c) for the $\Sigma Z=10$ events. Differences obtained with the corrected and uncorrected shifts for p, t, and ^{3}He fragments are indicated by the solid and open points, respectively. The error bars now correspond to just the statistical error. The larger systematic errors associated with the uncertainty in the energy calibrations are identical for both targets and hence cancel. The detector-bias corrections and their uncertainties are very similar for both targets and almost completely cancel as well. Even if all shifts were Coulomb in nature, then the subtraction procedure would still be a useful method of removing systematic errors. Furthermore, if the breakup separation is small, then effects due to the target's nuclear force will tend to cancel as well.

The differences follow the behavior expected for Coulomb accelerations: The four fragment types with $\Delta(Z/A)=0$ all have approximately zero difference, and particles with positive $\Delta(Z/A)$ values have positive differences, while those with negative values have negative differences. These observations provide *a posteriori* justification for the validity of the subtraction procedure. In fact, all data points can be fitted reasonably well with a straight line. The solid line in Fig. 9(c) is a least squares fit to the data for which the extracted breakup separation is 14.4 ± 1.5 fm. However, in principle different particle types need not be emitted at the same average breakup separation. Also, a fraction of the de-

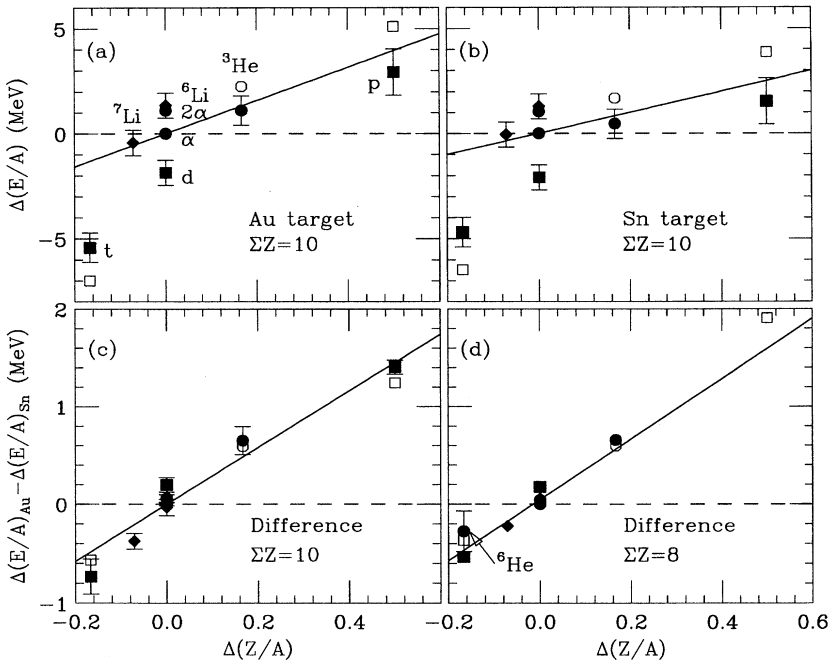

FIG. 9. (a) Average shifts between the fragment spectra in energy per nucleon for $\Sigma Z=10$ events obtained with the Au target as function of the relative Z/A ratio. (b) Average shifts obtained with the Sn target. (c) Differences between the shifts obtained with the Au and Sn targets for $\Sigma Z=10$ events. (d) Differences obtained for $\Sigma Z=8$ events. Shifts for hydrogen, helium, and lithium isotopes are indicated by the square, circular, and diamond shaped points, respectively. The open points have not been corrected for the detector bias.

tected particles does arise from the decay of long-lived intermediate states (Sec. V). The shift associated with such fragments will reflect Z/A values of their precursors present during the acceleration phase. For protons, tritons, and ^{3}He fragments, these precursors have Z/A values closer to 0.5 (Sec. V) and hence are associated with smaller absolute shifts. Therefore, the presence of such intermediates will decrease the magnitude of the observed shifts. The range of breakup separations consistent with the data is thus $R \leq 15.9$ fm. The consistency of the p, t, and ^{3}He data points with a single breakup separation in Fig. 9(c) is an indication that the sequential decay component is not the dominant component for these fragments.

Differences in the shifts are also plotted for $\Sigma Z=8$ events in Fig. 9(d). Note that a Coulomb shift is obtained for ^{6}He fragments from the $3\alpha+^6$He exit channel. The data follow the same trend as the $\Sigma Z=10$ events and a least squares fit (solid line) gives a similar breakup separation of 13.2 ± 1.5 fm. The point for the proton is not included in the fit (Sec. III). A value of $R=18\pm11$ fm was extracted from the proton velocity spectra for the $\Sigma Z=12$, $5\alpha+2p$ channel. This result is consistent with results for the other ΣZ values, but not very restrictive in and of itself.

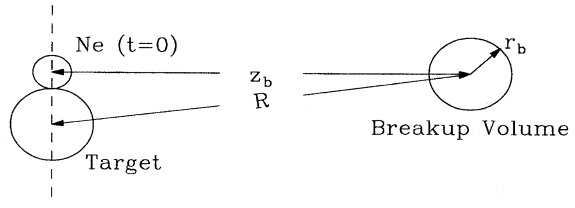

FIG. 10. Schematic representation of the position of the projectile fragments' breakup volume relative to the target.

For $R \leq 15.9$ fm, if the minimum projectile-target separation in the collision is the sum of their equivalent sharp radii, then the maximum distance traveled by the PLF from this point is $z_b=13$ fm for a peripheral trajectory. The relationship between z_b and R is shown schematically in Fig. 10. During this motion, the target and PLF may still be connected by some nuclear material. In any case, the time required to travel this distance is 1.6×10^{-22} s which is typical of time scales for direct processes. For comparison, statistical decay times were extrapolated from the decay-width systematics of Ref. [20]. Using the excitation energies in Table III, the average emission time for the first emitted particle is $3.1-6.2\times10^{-22}$ s. A lower limit of 7×10^{-22} s for the average emission time of all particles was obtained by assuming the decay width is constant for all decay steps. Even with this extreme assumption, this value is much larger than the experimental upper limit of 1.6×10^{-22} s and therefore presents strong evidence *against* a purely sequential-statistical projectile decay and again points to a more prompt decay process.

C. Residual shifts

Remembering that the difference in the shifts represents the equivalent shift for a $Z=29$ target, these differences can be scaled up appropriately for the Z values of the Au and Sn targets to give the Coulomb components of the measured shifts. The residual shifts, which are identical for each target by assumption, were obtained by subtracting out the Coulomb components. Average residual shifts obtained from both $\Sigma Z=8$ and 10 events are plotted in Fig. 11. For protons and ^{3}He fragments, the residual shifts are consistent with zero. However, the more neutron-rich isotopes of hydrogen and helium have large negative shifts. On the other hand, lithium and beryllium (2α) isotopes tend to favor positive

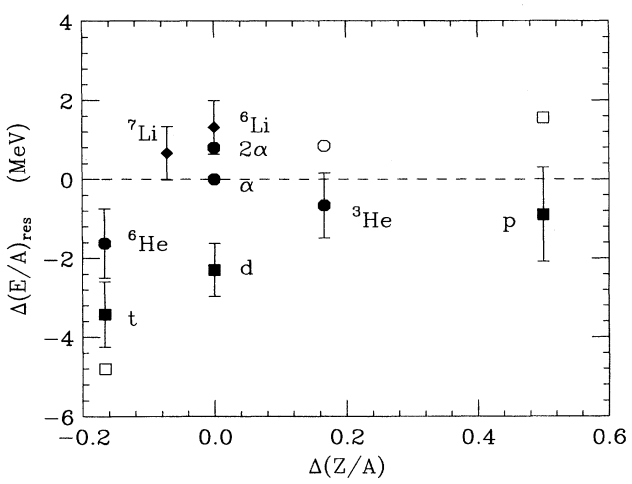

FIG. 11. Average residual shifts obtained for both $\Sigma Z=8$ and 10 events as a function of the relative Z/A ratio. The open data points have not been corrected for the detector bias.

residual shifts. Note that the systematic error for the 2α point is small. This is due to the fact that alpha particles, the reference particle, and 2α fragments share the same energy calibration.

The nonzero residual shifts indicate that the fragments were not emitted isotropically from the decaying PLF. Thus, the PLF did not achieve full equilibrium before decaying. As the time scale for equilibration is of the order of the time for a nucleon, at the Fermi surface, to cross the PLF (8×10^{-23} s), these residuals shifts are also consistent with the short PLF lifetime indicated by the magnitude of the Coulomb component. The fact that the more neutron-rich hydrogen and helium isotopes have slower longitudinal velocities suggests that they are formed out of the material produced by the mixing of projectile matter with the more neutron-rich target matter. In fact, if the projectile only skims the surface of the target nucleus, then it could interact with the neutron skin of the target (both targets have similar neutron skin thicknesses [21]), possibly producing a very neutron-rich neck in the intermediate velocity region.

V. CORRELATION FUNCTION

Final state interactions between the projectile fragments and the decay of intermediate states can be revealed through the construction of correlation functions. The two-body correlation function $1+R$ is defined as

$$\sigma_{12}(\mathbf{p}_1,\mathbf{p}_2)=(1+R)\sigma_1(\mathbf{p}_1)\sigma_1(\mathbf{p}_2), \tag{3}$$

where σ_{12} and σ_1 are the two-body and single-particle emission probabilities as function of the particle momenta $\mathbf{p}_{1,2}$. The above equation is often integrated over the total momentum of the two particles, $\mathbf{P}=\mathbf{p}_1+\mathbf{p}_2$, and the orientation of their relative momentum vector, $\mathbf{\Delta p}=\mu(\mathbf{p}_1/m_1-\mathbf{p}_2/m_2)$. The quantity $1+R$ can then be expressed as a function of $\Delta p=|\mathbf{\Delta p}|$. In practice, the integration of $\sigma_1(\mathbf{p}_1)\sigma_1(\mathbf{p}_2)$ is either performed or the quantity is obtained by event mixing; i.e., the distribution of relative momentum between particles from different events is determined.

An initial attempt to generate two-body and higher order correlation functions through event mixing was performed. Fake 5α events were created by randomly mixing alpha particles and sometimes 2α particles from different events. Background Δp spectra were then generated from these events. However, the $E_{\rm tot}$, velocity, and angular distributions of the PLF fragments reconstructed from these fake events were different from those found with real events. This resulted in the correlation functions being strongly distorted. For instance the correlation functions never approached a constant value (of magnitude close to unity) for large Δp values. Distortions such as these, but of much smaller magnitude, are observed in correlation functions obtained in other studies. Schapiro, DeAngelis, and Gross [22] explain these effects as resulting from conservation of energy and momentum. In the present case, the distortions are enhanced in magnitude as one is looking at correlations between fragments whose total mass represents a sizable fraction of the mass of the decaying system. Furthermore, for the Δp region of interest, one is not dealing with small angle correlations (defined by $\Delta p \ll P$).

Instead of event mixing, the background relative momentum distributions were obtained from the Monte Carlo simulations of Appendix A. Such distributions are appropriate as the goal of these simulations was to fit the single-particle distributions of the projectile fragments simultaneously with the velocity, $E_{\rm tot}$, and angular distribution of the reconstructed PLF. They contain no physics except momentum and energy conservation. There are no interactions between the fragments and no intermediate states except ^{8}Be(g.s.). However, the simulations do take into account the detector bias. The correlation function was determined by dividing the experimental relative momentum distribution by the simulated distribution. The simulated distribution was normalized to the same number of events as the experimental distribution; otherwise, no other normalization of the correlation function was performed to force it to approach unity at large Δp. The simulations of Appendix A should be considered as first generation, and by using them to construct the background one finds which correlations are absent in these simulations. Subsequently, second generation simulations will be created which include these absent correlations and fit the correlation functions. As a consistency check for these second generation simulations, the background relative momentum distributions constructed from the mixed simulated events were compared to, and found to be in agreement with, those from the mixed experimental events.

There are some important consequences of the adopted method.

(1) The Monte Carlo simulations balance momentum in the frame of the PLF and reproduce the experimental $E_{\rm tot}$ distributions. Hence, uninteresting correlations due to the conservation of energy and momentum are removed from the correlation function.

(2) The Monte Carlo–generated events were passed through the detector filter and hence both the simulated and experimental relative momentum distributions contain the same distortions due to the detector acceptance. Therefore, in dividing the experimental distribution by the simulated re-

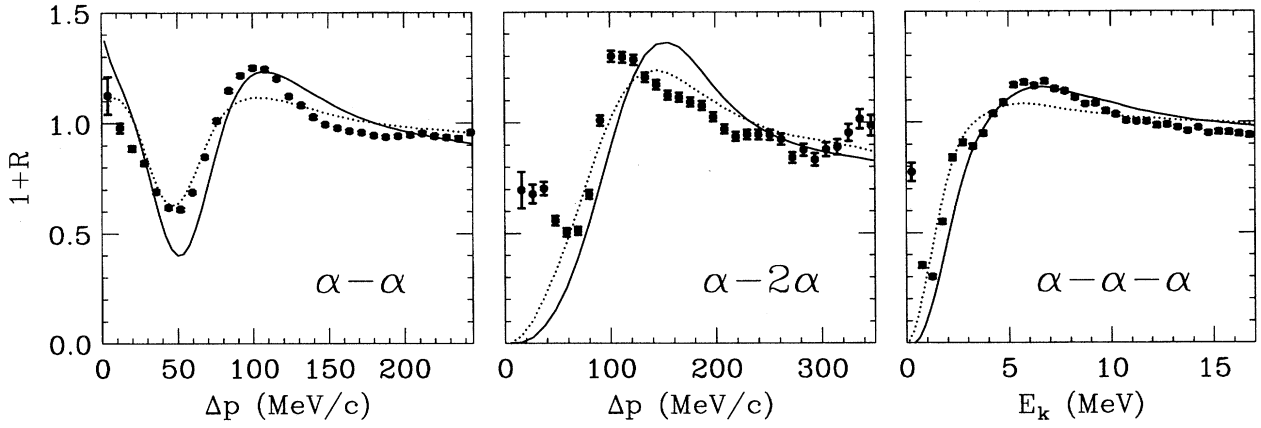

FIG. 12. Experimental correlation functions obtained for the 5α exit channel (data points). In comparison, predictions obtained from the trajectory calculations with breakup radii of 7 and 12 fm and no unstable intermediates besides the ^{8}Be ground state are indicated by the solid and dotted curves, respectively.

sults, these distortions are reduced in the ensuing correlation function. However, the resolution of the correlation function is still limited by the large solid angles of the MINIWALL detectors. Proper interpretation of the correlations functions will require additional Monte Carlo simulations (see later). Readers interested in the effect of the detector resolution on the correlation functions should contrast the results of this work with the inclusive correlation functions obtained with high resolution by Pochodzalla *et al.* [23].

(3) The Monte Carlo simulations include the decay of ^{8}Be(g.s.) fragments. Hence, the strong correlation associated with this decay is removed from the α-α correlation function. However, the inclusion of these particles allows correlations with the 2α fragments to be studied.

Higher order correlation functions are also constructed by a similar procedure. Instead of relative momentum, experimental and simulated distributions of the total kinetic energy E_k are divided. The quantity E_k is the total kinetic energy of the particles of interest in their center-of-mass frame. If all particles in the exit channel are included, then $E_k=E_{\rm tot}$. However, this correlation function always has the value of unity as the simulations were fitted to the experimental $E_{\rm tot}$ distributions.

Examples of two-, three-, and four-body correlation functions extracted from the 5α exit channel are shown in Figs. 12 and 13. For the α-α two-body correlation, each possible pair of alpha particles contributes to the final result. If there are no 2α fragments, then there are ten such pairs per 5α event. Similarly, for the higher order correlation, all possible combinations of the particles are considered. If there were no extra correlations between the projectile fragments apart from those introduced in the Monte Carlo simulations of Appendix A, then the correlation functions should be unity. Figures 12 and 13 clearly show that this is not the case.

Final state Coulomb interactions between projectile fragments will result in reduced correlations at small Δp or E_k. The decay of unstable intermediates or resonance final state interactions results in enhancement of the correlation function at the resonant energy. Symmetrization effects may also be important for correlations between identical particles. The magnitude of these effects depends on the spacial and temporal extent of the source of the fragments and they are often treated theoretically for two-body correlation functions using the Koonin-Pratt formalism [24–26]. Unfortunately, this quantum mechanical formalism is valid only in the limit that $\Delta p \ll P$ (small angle correlations) which is not fulfilled for the Δp region of interest in this work. Therefore, in an attempt to better understand the correlation functions, a classical trajectory approach was followed. The initial projectile fragments are randomly distributed within a spherical breakup volume of radius r_b located near the target as indicated in Fig. 10. The PLF has traveled along its peripheral trajectory a distance z_b from its first interaction with the target to this breakup configuration. The velocities of the fragments are again chosen as in Appendix A. The classical trajectories of all the fragments and the target nucleus are then followed under their mutual Coulomb interactions until their asymptotic velocities are approached.

As for the simulations in Appendix A, the probabilities for one and two ^{8}Be(g.s.) fragments were adjusted to reproduce the experimental probabilities of detecting one and two 2α fragments. The ^{8}Be probabilities obtained for the 5α exit channel are indicated by the dashed curves in Fig. 4. These results differ from those obtained in Appendix A (solid curves) where no interactions between the fragments were considered. The 2α probability is sensitive to these interactions as not all 2α fragments are produced by ^{8}Be(g.s.) decay. The component of the 2α probability which is not associated with ^{8}Be(g.s.) decay is reduced when interactions are included as the Coulomb repulsions increase the relative angles between such alpha particles. To compensate for this, a larger number of ^{8}Be(g.s) fragments was included in the present simulations to reproduce the experimental 2α probabilities. The Coulomb interactions also modify the velocity spectra of the fragments and so the parameters specifying the initial velocity distributions (Appendix A) were adjusted so that the final spectra reproduce the experimental results.

Examples of correlation functions obtained from this procedure are indicated by the solid curves in Fig. 12 for $r_b=7$ and 12 fm and $z_b=9.6$ fm. The peak at very small

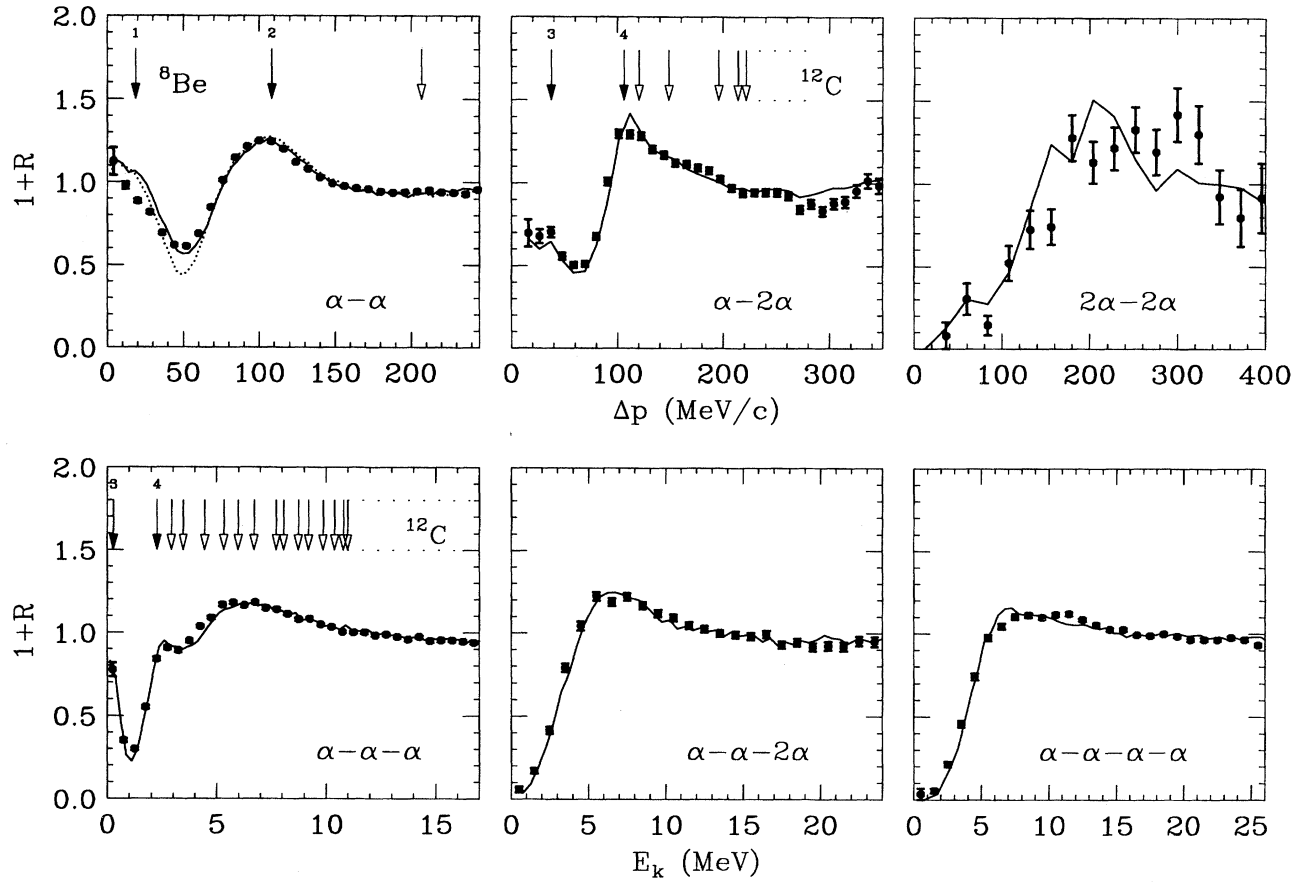

FIG. 13. Experimental correlation functions obtained for the 5α exit channel (data points). In comparison, fitted correlations functions obtained from trajectory calculations including unstable intermediates (as listed in Table VI) are indicated by the solid curves. The dotted curve shows the fit without any ^{9}Be decay. The arrows indicate the regions of the correlation function which can be associated with decay from states in the indicated nucleus. For the α-2α correlations, only known ^{12}C states which decay through ^{8}Be(g.s.) are indicated. States with the solid arrows were included in the fit and can be identified in Table VI by the labels on the arrows.

Δp values in the simulated α-α correlation is a result of the increased number of ^{8}Be(g.s.) fragments in the new simulation. Otherwise the predicted correlations are suppressed at small Δp (or E_k), forming a "Coulomb hole." They quickly rise, overshoot, and then approach unity (approximately) at the larger Δp and E_k values.

To understand the nature of this overshoot feature, the reader is referred to Fig. 14 which shows the correlation function predicted for three $E_{\rm tot}$ values. To simplify this discussion, no unstable states and no target nucleus were included in the trajectory calculations. For $E_{\rm tot}$=20 MeV (dashed curve), the total initial Coulomb energy of the five alpha particles represent a sizable fraction of $E_{\rm tot}$. This results in the substantial modification of the fragment velocities, suppressing events with small relative momenta and increasing events with intermediate values. Because of conservation of momentum and energy, the largest values of Δp and E_k occur in events which also contain the smallest values. For example, the largest Δp between two alpha particles (273 MeV/c) occurs when the other three alpha particles are all at rest. Suppression of small Δp and E_k therefore also leads to a suppression of the largest values as indicated by the dashed curve. Figure 14 also shows the results for $E_{\rm tot}$=100 and 500 MeV (dotted and solid curves, respectively). For these cases, the initial Coulomb energy represents only a small fraction of $E_{\rm tot}$ and the Δp region of the figure is associated with smaller relative angles. Not surprisingly, the result for the largest $E_{\rm tot}$ value approaches the Koonin-Pratt prediction (for Coulomb interactions only) as indicated by the open points. As the experimental $E_{\rm tot}$ values are closer to the 20 MeV calculation (see Fig. 3), the predicted correlation functions in Fig. 12 display the overshoot feature. The suppression at large Δp and E_k values is not observed as, at these values, the relative momentum distributions are dominated by events with the largest $E_{\rm tot}$ values.

Although the predictions with Coulomb interactions do reproduce some of the features of the experimental correlation functions, overall they do not fit the data very well, no matter what breakup radius is chosen. The deviations from these predictions can be explained as due to decay of unstable intermediates. In the simulation, these were included with the other projectile fragments in the breakup volume and then subsequently allowed to decay. For unstable states with short half-lives ($\Gamma >$ 100 keV), trajectories were fol-

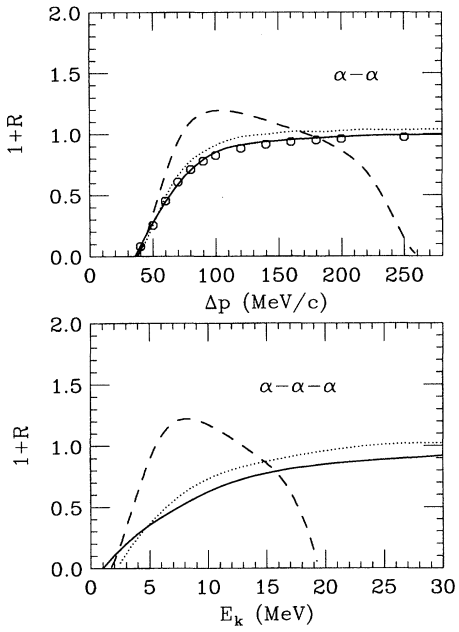

FIG. 14. Two- and three-body correlation functions obtained for the 5α exit channel using trajectory calculations assuming only Coulomb interactions and no unstable intermediates. The results obtained for total excitation energies of 20, 100, and 500 MeV and a breakup radius of 8.5 fm are indicated by the dashed, dotted, and solid curves, respectively. At the largest excitation energy, the result approaches the prediction of the Koonin-Pratt formalism indicated by the circular points.

lowed for a time period selected from the appropriate exponential distribution. The trajectories of the decay products were then determined, taking into account their Coulomb interactions with all other fragments. The line shape of the decays was assumed to be Lorentzian with widths taken from Refs. [27,28]. Exceptions to this were made for some wide states in which the decay channel is just above its threshold. For the states listed in Table V, the R-matrix line shape for an isolated resonance [32] is multiplied by a microcanonical phase space factor [Eq. (9) of Ref. [33]]. The phase space factor ensures that the maximum energy released in the decay does not extend past $E_{\rm tot}$, the total kinetic energy of the channel. For longer-lived intermediates, interactions of the decay products with the other fragments were ignored.

Intermediates which decay into three or more fragments were treated as a series of sequential two-body decays. For the decay of ^{6}Be(g.s.), ^{9}Be(1.68 MeV), and ^{9}B(2.36 MeV) which pass through the wide ^{5}He or ^{5}Li ground states, the sequential decay was treated as in Refs. [23,32].

Experimental and fitted correlation functions obtained for the seven most abundant $\Sigma Z=10$ exit channels are displayed in Figs. 13–21 and the fitted multiplicities of unstable intermediates are listed in Tables VI–XII. The correlations between alpha particles are very similar to those found for the 5α channel and only a few examples of these are shown in the other figures.

TABLE V. Excited states for which the R-matrix formalism was used to determine the line shape. The R-matrix parameters were obtained from the listed references.

State	Reference
^{8}Be 3.01 MeV	[29]
^{5}Li g.s.	[30]
^{5}He g.s.	[30]
^{4}He 20.01 MeV	[31]

A. 5α exit channel

For the 5α exit channel, the experimental correlation functions were fitted by including five intermediate states (multiplicities listed in Table VI) into the simulation. The fits are given by the solid curves in Fig. 13 and the solid arrows indicate the mean Δp or E_k values associated with the included states. In producing these fits, we again note that the fragment velocity distributions and the 2α probability curve are modified by including these intermediates and hence had to be refitted. The breakup radius was also varied to achieve the displayed fits and its value will be discussed later. There was little or no sensitivity of the fits to z_b. The errors listed in Table VI show the range over which reasonable fits were obtained (the fitting process was too time consuming to perform a χ^2 analysis of the errors).

The rise in the α-α correlation function indicated by the arrow labeled "2" is explained in the simulations by a combination of the overshoot feature due to the Coulomb interactions plus contributions from the decay of the wide first excited state of ^{8}Be. There is no indication for the presence of higher excited states, although the very wide ($\Gamma=1.5$ MeV) second excited state (first open arrow) would be difficult to see unless it had a substantial multiplicity.

The ^{9}Be(2.43 MeV) state decays predominantly (94%) via $\alpha+^{5}\mathrm{He}\rightarrow 2\alpha+n$. The two alpha particles from this decay

TABLE VI. Multiplicity of intermediate states obtained from fitting the experimental correlation functions for the 5α exit channel with the Sn target. The superscript number for each state refers to the arrows in Fig. 13 which show the region of the correlation function that these states populate. The exclusive multiplicities are the multiplicities of each intermediate that were included in the simulation. The inclusive values also include the multiplicity of such states which were produced in the sequential decay of other intermediates. The total multiplicity and fraction of alpha particles originating from sequential decay are also listed.

State(s)	Multiplicity exclusive	Multiplicity inclusive
^{8}Be g.s.[1]	0.43±0.04	0.60±0.06
^{8}Be 3.04 MeV[2]	0.76±0.15	
^{9}Be 2.43 MeV[a]	0.092±0.018	
^{12}C 7.65 MeV[3]	0.037±0.006	
^{12}C 9.64 MeV[4]	0.128±0.019	
total	1.44±0.24	
Particle	**Multiplicity**	**Fraction**
α	3.04±0.50	0.61±0.10

[a]Multiplicity only for decay into $\alpha+^{5}$He exit channel.

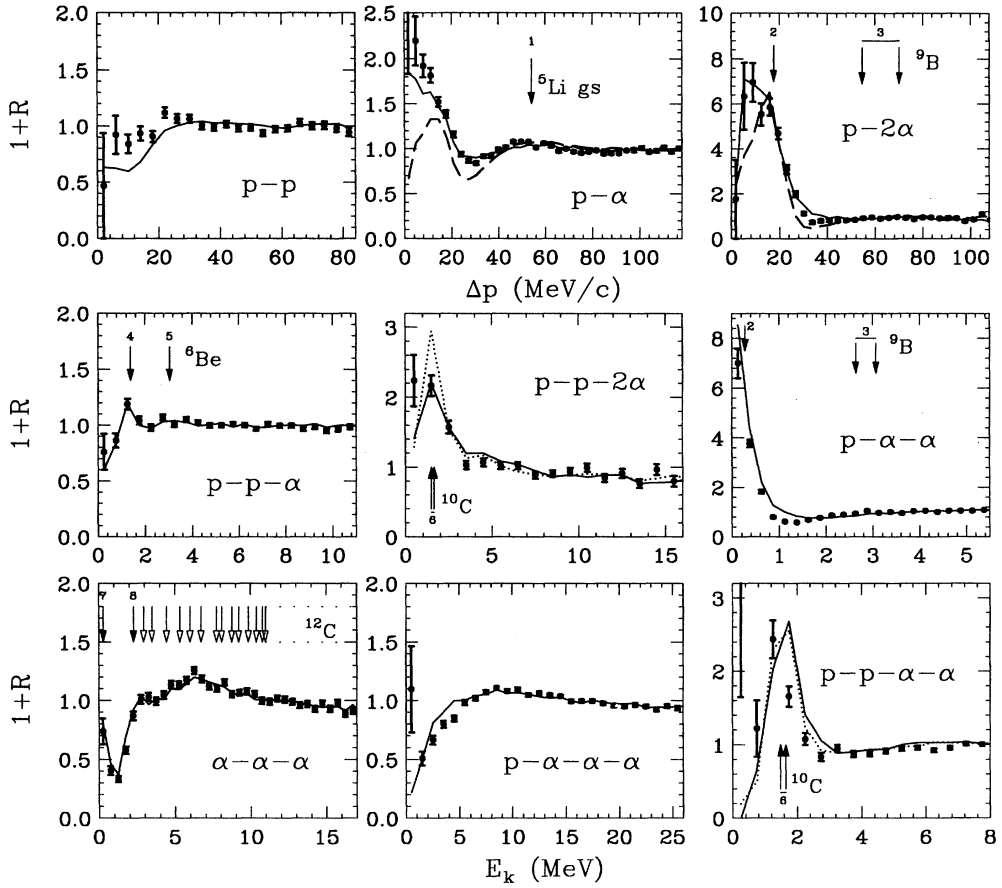

FIG. 15. Experimental correlation functions obtained for the $4\alpha+2p$ exit channel (data points). In comparison, fitted correlations functions obtained from trajectory calculations including unstable intermediates (as listed in Table VII) are indicated by the solid curve. The dashed curves show the fits to the p-α and p-2α correlation functions obtain when ^{9}B(g.s.), but no ^{10}B decay, was assumed. The dotted and solid curves were obtained for the p-p-2α and p-p-α-α correlations assuming the ^{10}C states decay through ^{9}B(g.s.) and ^{6}Be(g.s.) levels, respectively. The arrows indicate the position of structures associated with intermediates listed in Table VII.

should be associated with a broad peak in the α-α correlation function at $\Delta p \approx 50$ MeV/c [23]. Because of the poor resolution of the experimental apparatus, this feature cannot be resolved from other structures in the correlation function. However, a better fit (solid curve) to the experimental data was obtained by including a small amount of this state. In contrast, the prediction obtained without this state is shown by the dotted curve. The ^{9}Be(2.43 MeV) state also decays through ^{8}Be(g.s.) as do other ^{9}Be states and these will contribute to the measured ^{8}Be multiplicity.

The α-2α and α-α-α correlations show structures originating from the decay of ^{12}C states. These structures are

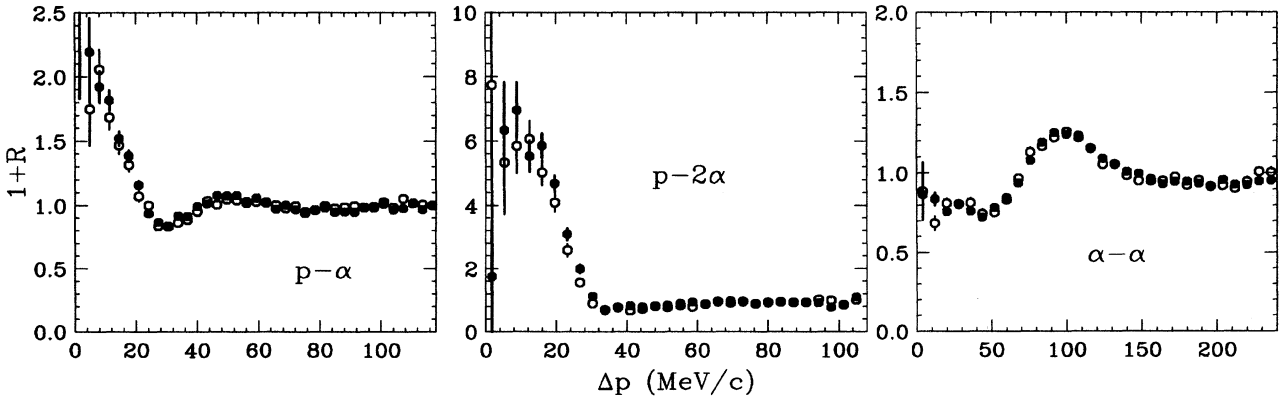

FIG. 16. Comparison of experimental correlations function obtained with the Sn (solid points) and Au (open points) targets for the $4\alpha+2p$ exit channel.

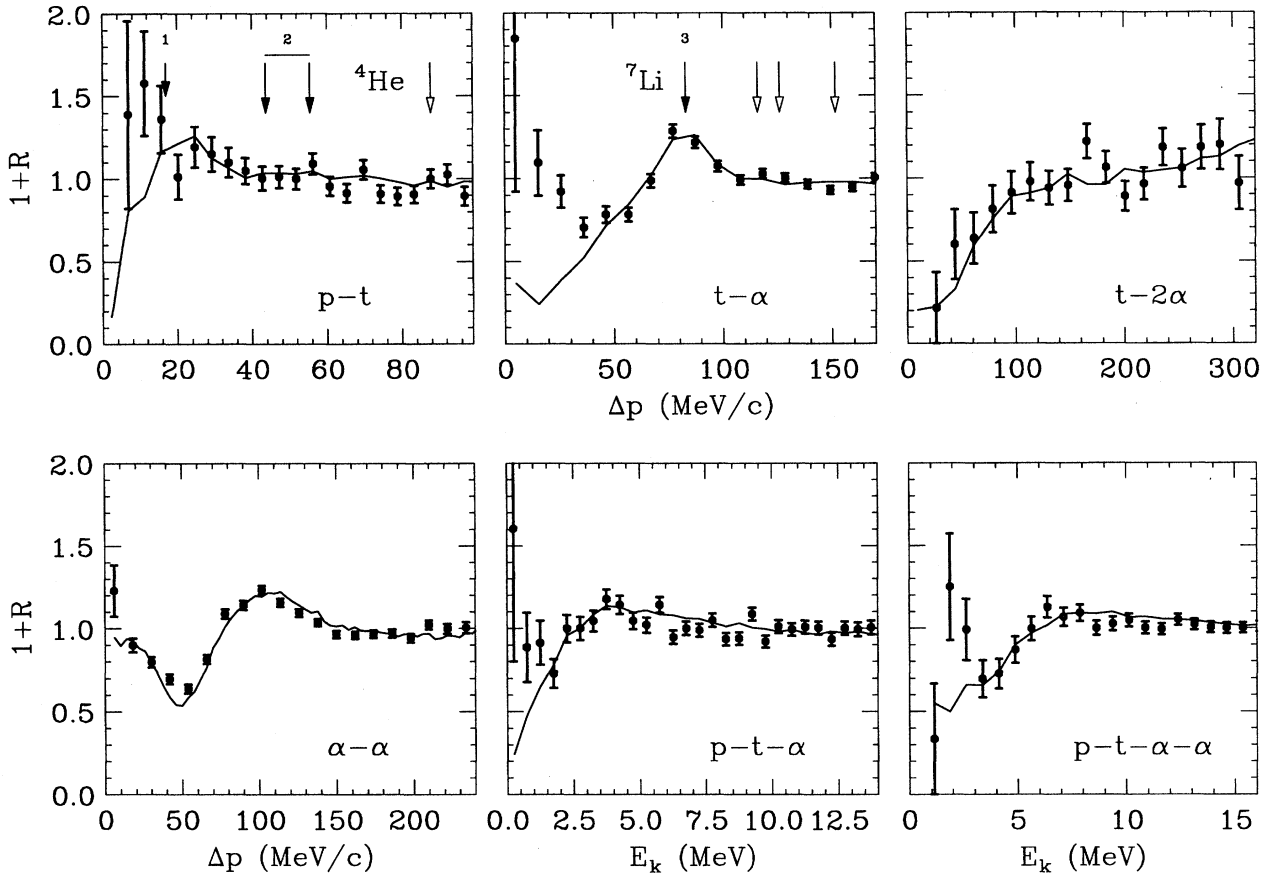

FIG. 17. Experimental and simulated correlation functions obtained for the $4\alpha+p+t$ exit channel. The arrows indicate the position of structures associated with intermediates listed in Table VIII.

again superimposed on regions of the correlation function which are modified by the Coulomb interactions. Arrow 3 indicates the position of the 7.65 MeV state which sits in a Coulomb hole. Although this state in very narrow ($\Gamma=8.5$ eV), due to the experimental resolution it becomes a rather broad structure in the α-2α correlation function. The next excited state of ^{12}C at 9.65 MeV (arrow 4) modifies the overshoot structure produced by the Coulomb interactions.

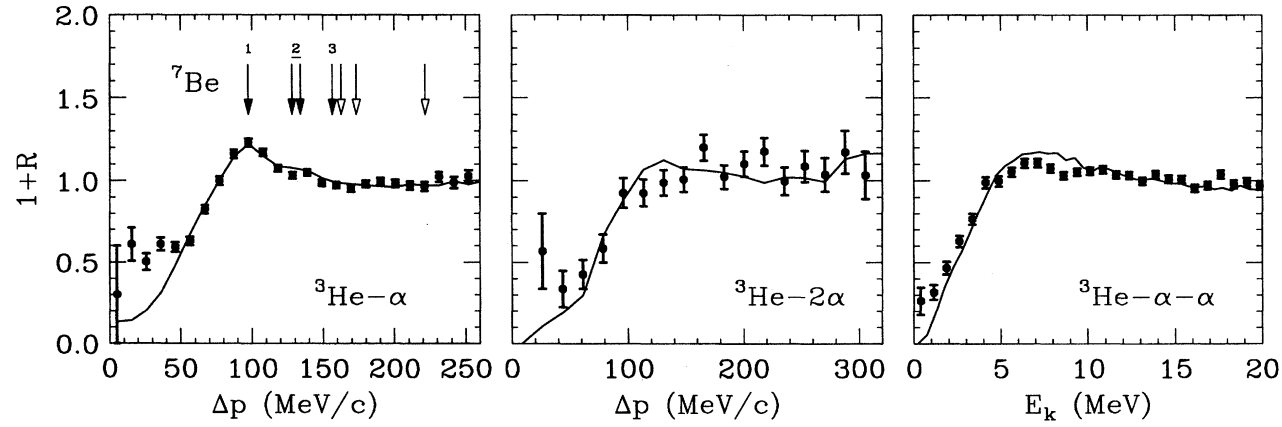

FIG. 18. Experimental and simulated correlation functions obtained for the $4\alpha+^3$He exit channel. The arrows indicate the position of structures associated with intermediates listed in Table IX.

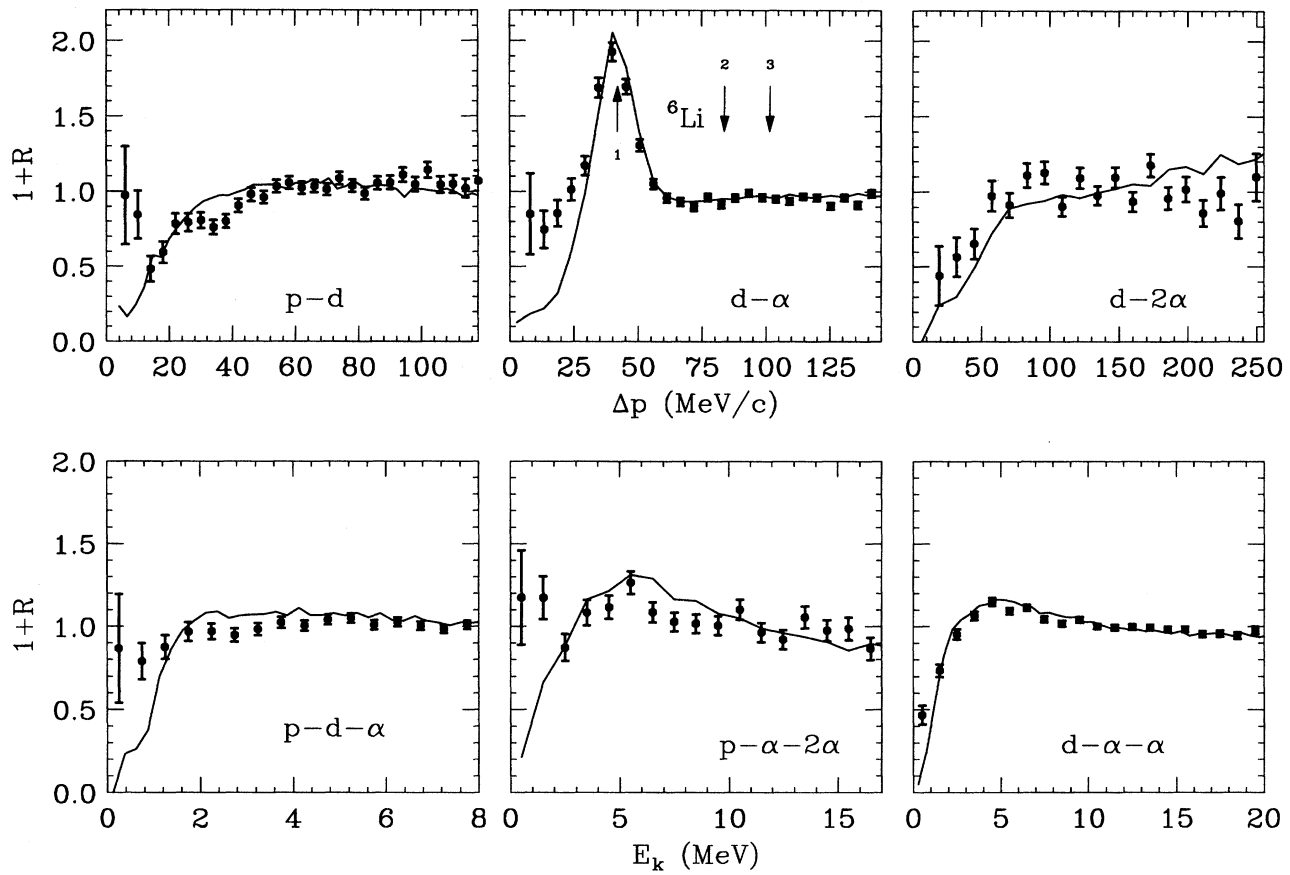

FIG. 19. Experimental and simulated correlation functions obtained for the $4\alpha+p+d$ exit channel. The arrows indicate the position of structures associated with intermediates listed in Table X.

However, it should be noted that this state starts a region of many closely spaced levels (open arrows in Fig. 13) which can decay to three alpha particles. Because of the experimental resolution, these states cannot be resolved and may provide a smooth contribution to these correlation functions. There are also many ^{16}O levels which may contribute in a similar way to the α-α-2α and α-α-α-α correlation functions. Therefore, the total multiplicity of unstable states listed in Table VI must be taken as a lower limit. In the simulations, ^{8}Be(g.s) fragments were included directly or result from the decay of the ^{12}C states. Hence, in Table VI, both an inclusive (from all sources) and an exclusive (directly included) ^{8}Be(g.s) multiplicity are listed. However, as noted above, the latter may have contributions from the decay of ^{9}Be states.

B. $4\alpha+2p$ exit channel

The correlation functions obtained for the $4\alpha+2p$ exit channel, shown in Fig. 15, display a rich variety of structure. The experimental p-p correlation function is rather flat. In the simulation, only a small suppression at low Δp values is obtained; the Coulomb hole is largely filled due to the number of sequentially emitted protons (see later). However, the experimental result still shows a small enhancement over the simulation at low Δp. The attractive singlet S-wave interaction between two protons, which was not included in the simulation, is probably the cause of this enhancement.

The p-α, p-2α, and p-α-α correlations show very large enhancements at small Δp values, completely filling in any Coulomb holes. For other reactions, similar p-α correlations have been attributed to the decay ^{9}B(g.s.)$\rightarrow p+^8$Be(g.s.) $\rightarrow p+\alpha+\alpha$ [23]. However, the decay of this state alone, as indicated by the dashed curves, cannot account for the complete shape of the correlation function. In particular, this decay cannot explain the enhancements at the very lowest Δp values in both the p-α and p-2α correlations. In the fit, both ^{9}B(g.s.) and the decay sequence ^{10}B$\rightarrow p+^9$Be(1.69 MeV) $\rightarrow p+n+^8$Be(g.s.) $\rightarrow p+n+\alpha+\alpha$ were included. The neutron emitted from the decay of ^{9}Be(1.69 MeV) in the above sequence has very little energy and so the recoil to the resulting ^{8}Be fragment is minimal. Thus, kinematically the ^{9}B and ^{10}B decays are very similar. To produce the correlations at very small Δp, the excitation energy for the ^{10}B level must be just above, or straddle, the 8.28 MeV threshold for the decay. The wide 8.07 MeV ($\Gamma=0.8$ MeV) state would be a good candidate and was included in the simulation and contributed to an improved fit not only at the very small Δp values, but because of its width, to Δp values out to $\approx$30 MeV/c for both p-α and p-2α pairs. Alternatively, a narrow unknown level in ^{10}B at slightly higher energy can-

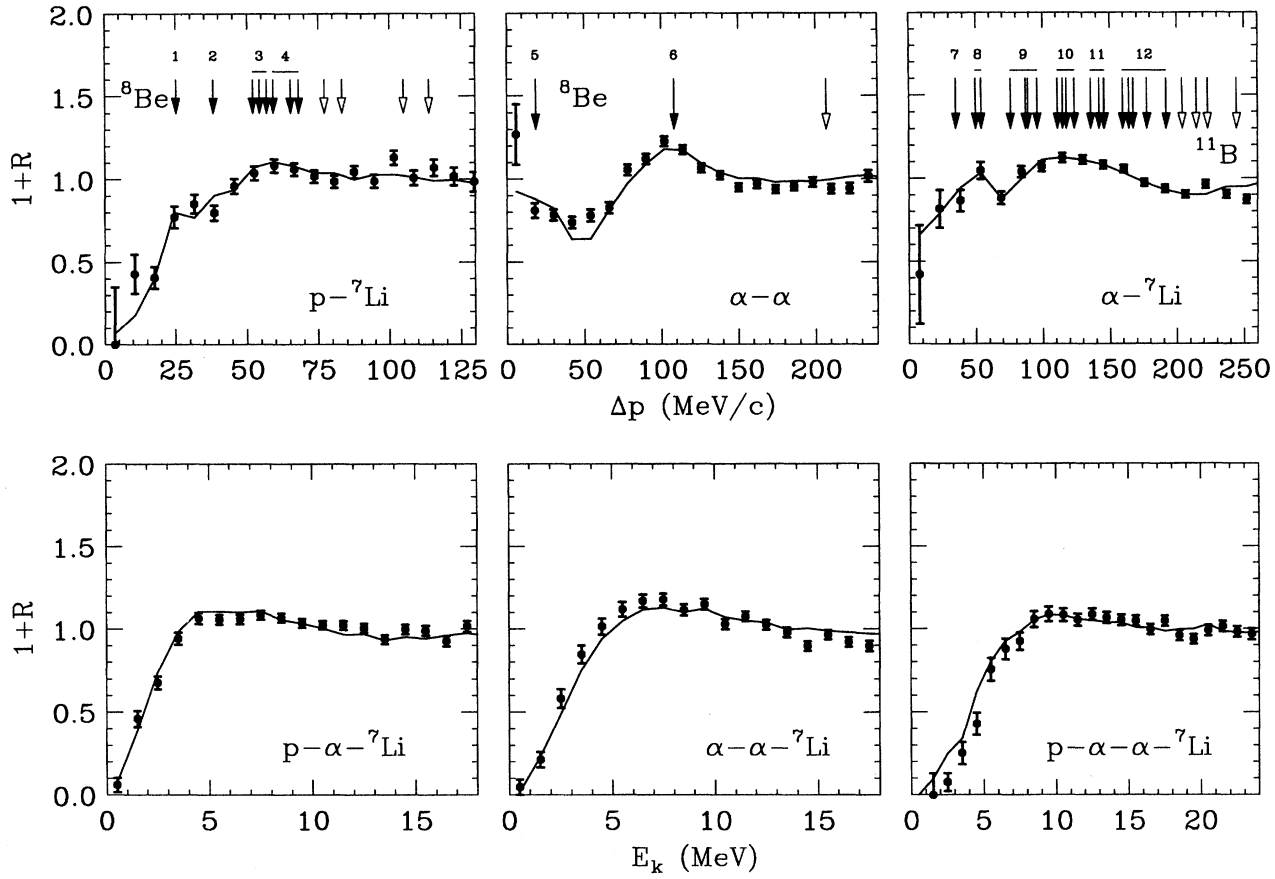

FIG. 20. Experimental and simulated correlation functions obtained for the $3\alpha+p+{}^7$Li exit channel. The arrows indicate the position of structures associated with intermediates listed in Table XI.

not be ruled out. In this case, decay from the narrow 8.894 MeV level ($\Gamma=84$ keV) of ^{10}B could also be invoked to improve the fit at $\Delta p\approx 30$ MeV/c. This would result in a different ratio between ^{9}B and ^{10}B and so in Table VII their multiplicities have been summed together.

There is also a small, but broad, rise in the experimental p-α correlation function at the position associated with ^{5}Li $\rightarrow p+\alpha$ decay (arrow 1). However, in the simulation this rise can be largely explained by a Coulomb overshoot feature. In Table VII only a limit is listed for this state. Unfortunately, p-α pairs from the decay of ^{5}Li are located near the maximum in the Δp distribution and so the correlation function is not very sensitive to their presence.

The existence of other proton-emitting intermediates can be seen in the p-p-2α and p-p-α-α correlation functions. The peaks in these correlations are at approximately the right position to be associated with either, or both, of the known ^{10}C excited states at 5.22 and 5.38 MeV (arrow 6). The mode of decay of these states is unknown, but in the simulation two sequential decay sequences starting with either $p+{}^9$B(g.s.) or $\alpha+{}^6$Be(g.s.) were considered. These two possibilities are indicated by the dotted and solid curves, respectively. The $p+{}^9$B(g.s.) decay overestimates the p-p-2α yield a little and so the $\alpha+{}^6$Be(g.s.) decay is the favored explanation. This decay also reproduces the peak in the p-p-α correlation associated with decay of the ^{6}Be(g.s.) fragment (arrow 4). For either decay sequence, the peaks in the experimental p-p-α-α and p-p-2α correlation functions would be better reproduced if the ^{10}C excitation energy was slightly lower.

Examples of the dependence of the experimental correlation functions on the target are shown in Fig. 16. Within the experimental errors, the data points are identical for the two targets. This result is typical of that found for all other exit channels. A closer examination of the influence of the target nucleus on the correlations is provided in Sec. V I.

C. $4\alpha+p+t$ exit channel

The correlation functions obtained for the $4\alpha+p+t$ exit channel are displayed in Fig. 17. The p-t correlation function shows a general enhancement for low Δp values. Part of this enhancement can be attributed to the decay of the first (arrow 1) and higher (arrow 2) excited states of an α. However, the simulation was not able to reproduce the experimental yield at the lowest values of Δp. The peak in the t-α correlation function is associated with the decay of the ^{7}Li(4.63 MeV) state (arrow 3), but again the simulation was not able to reproduce the experimental yield for lower Δp values. Similarly the filled-in Coulomb hole for the p-t-α correlation

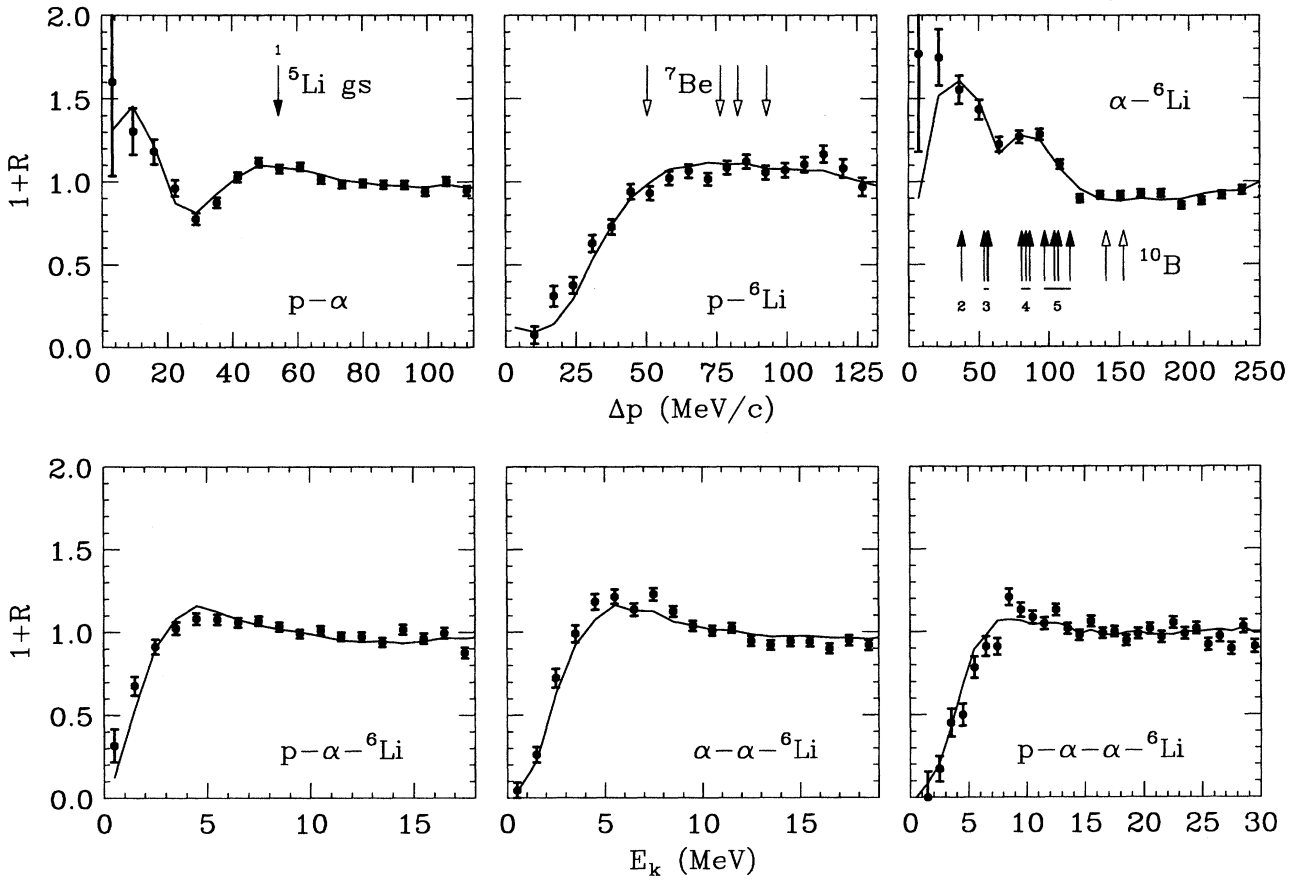

FIG. 21. Experimental and simulated correlation functions obtained for the $4\alpha+p+{}^{6}$Li exit channel. The arrows indicate the position of structures associated with intermediates listed in Table XII.

function was not reproduced. The multiplicities associated with the extra experimental yield, relative to the simulations, are listed in Table VIII (inclusive). They are all very small and have large statistical errors. These excesses are not all independent as an excess p-t-α yield results in excess p-t and t-α yields. Subtracting off the contribution from the higher order correlations, the exclusive excess multiplicities are also listed in Table VIII. The entire excess p-t multiplicity may be accounted for by the excess p-t-α multiplicity. A possible candidate for this excess multiplicity would be the decay of an α-α^* state of ^{8}Be. The α^* represent the first excited state of an alpha particle and such ^{8}Be states are predicted to constitute a rotational band. The 0^+ bandhead is expected to be located just above the threshold for the α-α^* decay [34,35] and thus its decay would enhance the region of low E_k in the p-t-α correlation function. Whether it could also enhance the region of excess p-t yield is not known; this discrepancy may be just a result of the uncertainty in the $\alpha^*\rightarrow p+t$ line shape.

The excess t-α multiplicity could be associated with the 5.4 MeV state of ^{8}Li if it is assumed to have a $t+{}^{5}$He decay branch. This decay was simulated and was found to populate the appropriate Δp region. An alternative explanation for the excess multiplicities is that the space-time extent for the source of tritons is separate from that for protons and alpha

TABLE VII. As for Table VI, but for the $4\alpha+2p$ exit channel. For states in which only an upper limit was determined, the displayed fit in Fig. 15 was obtained with half of the limiting value.

State(s)	Multiplicity exclusive	Multiplicity inclusive
^{5}Li g.s.[1]	≤ 0.40	
^{6}Be g.s.[4]		0.021 ± 0.004
^{6}Be 1.67 MeV[5]	≤ 0.023	
^{8}Be g.s.	0.19 ± 0.02	0.51 ± 0.06
^{8}Be 3.04 MeV	0.46 ± 0.09	
^{9}Be 2.43 MeV[a]	0.031 ± 0.006	
^{9}B g.s.[2], ^{10}B >8.27 MeV	0.26 ± 0.04	
^{9}B 2.36,2.79 MeV[3]	≤ 0.048	
^{10}C 5.22,5.38 MeV[6]	0.021 ± 0.004	
^{12}C 7.65 MeV[7]	0.017 ± 0.003	
^{12}C 9.64 MeV[8]	0.037 ± 0.006	
total	1.25 ± 0.40	
Particle	**Multiplicity**	**Fraction**
α	2.61 ± 0.64	0.65 ± 0.16
p	0.55 ± 0.29	0.28 ± 0.14

[a]Multiplicity only for decay into $\alpha+{}^{5}$He exit channel.

TABLE VIII. As for Table VII, but for the $4\alpha+p+t$ exit channel. For the correlations in which the simulation could not fit the experimental data at low Δp or E_k values, the excess experimental multiplicities are also listed.

State(s)	Multiplicity exclusive	Multiplicity inclusive
^{4}He 20.01 MeV[1]	0.037±0.007	
^{4}He 21.18,22.01 MeV[2]	≤ 0.021	
^{5}Li g.s.	≤ 0.26	
^{7}Li 4.63 MeV[3]	0.123±0.018	
^{8}Be g.s.	0.205±0.020	0.40±0.04
^{8}Be 3.04 MeV	0.45±0.09	
^{9}B g.s., ^{10}B >8.27 MeV	0.126±0.019	
^{9}B 2.36,2.79 MeV	≤0.087	
^{12}C 7.65 MeV	0.015±0.002	
^{12}C 9.64 MeV	0.051±0.008	
(p-t)	0.000±0.002	0.003±0.002
(t-α)	0.011±0.006	0.017±0.006
(p-t-α)	0.0026±0.0015	0.0050±0.0015
(p-t-α-α)	0.0012±0.0006	
total	1.28±0.38	
Particle	Multiplicity	Fraction
α	2.18±0.56	0.55±0.14
p	0.37±0.23	0.37±0.23
t	0.26±0.08	0.26±0.08

particles. This would lead to a reduction in the Coulomb interactions between these particles, resulting in a diminished Coulomb hole. Please note that the magnitude of the Coulomb holes in these simulations was determined by adjusting the breakup radius to reproduce the correlations involving only alpha particles. An excess multiplicity is observed in the p-t-α-α correlations and may be associated with ^{12}C state(s) with excitation energy near 27 MeV.

TABLE IX. As for Table VIII, but for the $4\alpha+^3$He exit channel.

State(s)	Multiplicity exclusive	Multiplicity inclusive
^{7}Be 4.57 MeV[1]	0.099±0.015	
^{7}Be 6.73,7.21 MeV[2]	≤ 0.041	
^{7}Be 9.27[3]	≤ 0.013	
^{8}Be g.s.	0.319±0.032	0.40±0.04
^{8}Be 3.04 MeV	0.58±0.11	
^{9}Be 2.43 MeV	0.079±0.016	
^{12}C 7.65 MeV	0.017±0.003	
^{12}C 9.64 MeV	0.062±0.009	
(^{3}He-α)	0.024±0.004	
total	1.20±0.22	
Particle	Multiplicity	Fraction
α	2.33±0.38	0.58±0.10
^{3}He	0.15±0.05	0.15±0.05

[a]Multiplicity only for decay into $\alpha+^5$He exit channel.

TABLE X. As for Table VIII, but for the $4\alpha+p+d$ exit channel.

State(s)	Multiplicity exclusive	Multiplicity inclusive
^{5}Li g.s.	≤ 0.26	
^{6}Li 2.19 MeV[1]	0.236±0.035	
^{6}Li 4.31 MeV[2]	≤ 0.050	
^{6}Li 5.65 MeV[3]	≤ 0.038	
^{8}Be g.s.	0.264±0.026	0.46±0.05
^{8}Be 3.04 MeV	0.57±0.11	
^{9}Be 2.43 MeV[a]	0.022±0.004	
^{9}B g.s., ^{10}B >8.27 MeV	0.122±0.018	
^{9}B 2.36,2.79 MeV	≤0.060	
^{12}C 7.65 MeV	0.017±0.002	
^{12}C 9.64 MeV	0.044±0.007	
(p-d)		0.0024±0.0007
(d-α)	0.015±0.003	
(p-d-α)	0.0027±0.0008	
(p-α-2α)	0.005±0.002	
total	1.49±0.41	
Particle	Multiplicity	Fraction
α	2.47±0.54	0.62±0.14
p	0.26±0.15	0.26±0.15
d	0.29±0.08	0.29±0.08

[a]Multiplicity only for decay into $\alpha+^5$He exit channel.

D. $4\alpha+^3$He exit channel

The $4\alpha+^3$He exit channel shows the presence of ^{7}Be(4.57 MeV) decay in the ^{3}He-α correlation function (arrow 1) of Fig. 18. However, like the t-α correlation, there is excess yield relative to the simulations at the lowest Δp values. The excess multiplicities are again small and listed in Table IX. One possibility that was investigated is that this excess results from 5α events in which one alpha particle was incorrectly identified as a ^{3}He fragment. Such incorrect identifications would enhance the low Δp region as the α-α correlation has a strong enhancement due the decay of ^{8}Be(g.s.). The α-^{3}He separation of the MINIWALL detectors becomes difficult at low energies and this resulted in the imposition of a 13 MeV/nucleon threshold above which the separation was judged adequate. To investigate the multiplicity of these contaminated events, low energy alpha particles in the simulated 5α events were treated as ^{3}He fragments. The predicted ^{3}He-α correlation function for such events exhibits a sharp peak at $\Delta p \approx 0$ MeV/c unlike the experimental results. An upper limit of 3% was placed on such contaminated events for all Δp values. Similar to the $4\alpha+p+t$ exit channel, the excess multiplicities may result either from a separation between the ^{3}He and α sources or from the decay of a ^{8}Be level.

E. $4\alpha+p+d$ exit channel

The d-α correlation associated with the ^{6}Li(2.19 MeV) state (arrow 1) is very prominent in the results obtained for the $4\alpha+p+d$ exit channel displayed in Fig. 19. Similar to the previous two exit channels, there is excess yield at low Δp associated with the p-d, d-α, and p-d-α correlations.

TABLE XI. As for Table VIII, but for the $3\alpha+p+{}^{7}$Li exit channel.

State(s)	Multiplicity exclusive	Multiplicity inclusive
^{5}Li g.s.	$\leqslant 0.34$	
^{8}Be g.s.[5]	0.114 ± 0.011	0.22 ± 0.02
^{8}Be 3.04 MeV[6]	0.24 ± 0.05	
^{8}Be 17.64 MeV[1]	0.020 ± 0.010	
^{8}Be 18.15 MeV[2]	0.019 ± 0.010	
^{8}Be 18.91,19.07, 19.24 MeV[3]	0.021 ± 0.011	
^{8}Be 19.4,19.86, 20.1 MeV[4]	0.010 ± 0.005	
^{9}B g.s., ^{10}B >8.27 MeV	0.060 ± 0.009	
^{9}B 2.36,2.79 MeV	$\leqslant 0.047$	
^{11}B 8.92 MeV[7]	0.012 ± 0.002	
^{11}B 9.18,9.27 MeV[8]	0.073 ± 0.014	
^{11}B 9.87,10.26, 10.33,10.59 MeV[9]	0.103 ± 0.020	
^{11}B 11.26,11.44, 11.58,11.88 MeV[10]	0.087 ± 0.017	
^{11}B 12.55,12.91, 13.13,13.16 MeV[11]	0.078 ± 0.015	
^{11}B 14.04,14.34,14.56, 15.32,16.43 MeV[12]	0.051 ± 0.013	
^{12}C 7.65 MeV	0.0038 ± 0.0006	
^{12}C 9.64 MeV	0.015 ± 0.002	
total	1.10 ± 0.38	
Particle	Multiplicity	Fraction
α	1.51 ± 0.45	0.50 ± 0.15
p	0.32 ± 0.24	0.32 ± 0.24
^{7}Li	0.47 ± 0.11	0.47 ± 0.11

For p-d pairs, this excess is associated with a small peak in the Coulomb hole which has been seen before and attributed to interactions of the proton and deuteron with the Coulomb field of the residue (target) [23]. However, this field is included in the present simulations and, no matter what target-projectile breakup separation was assumed, no similar structure could be produced. It was impossible to reproduce the excess yields by the decay of known ^{7}Be states. Possibly, the excess yields could again be associated with the decay of a ^{8}Be state. There is some indication of excess yield in the p-α-2α correlations. This is somewhat puzzling as no similar feature was observed in p-α-2α correlations for other exit channels.

F. $3\alpha+p+{}^{7}$Li and $3\alpha+p+{}^{6}$Li exit channels

The results for the $4\alpha+p+{}^{7}$Li and $4\alpha+p+{}^{6}$Li exit channels are displayed in Figs. 20 and 21. Of interest are the presence of ^{11}B and ^{10}B decays in the α-^{7}Li and α-^{6}Li correlation functions, respectively. Also there are indications of ^{8}Be states associated with p-^{7}Li pairs. There is no evidence for any ^{7}Be states in the p-^{6}Li correlations, although a small contribution cannot be excluded. In fact, the p-^{6}Li is the only two-body correlation function for which there are no obvious extraneous features besides the Coulomb hole. Note that the small rise in the p-d correlation function at $\Delta p\sim 0$ is not observed in the p-^{6}Li correlations. If this rise is due to interactions with the target, then it equally well might be expected to occur for p-^{6}Li pairs.

TABLE XII. As for Table VIII, but for the $3\alpha+p+{}^{6}$Li exit channel.

State(s)	Multiplicity exclusive	Multiplicity inclusive
^{5}Li g.s.[1]	$\leqslant 0.30$	
^{8}Be g.s.	0.094 ± 0.009	0.20 ± 0.02
^{8}Be 3.04 MeV	0.25 ± 0.05	
^{9}B g.s., ^{10}B >8.27 MeV	0.071 ± 0.011	
^{9}B 2.36,2.79 MeV	$\leqslant 0.050$	
^{10}B 4.77 MeV[2]	0.071 ± 0.011	
^{10}B 5.11,5.16,5.18 MeV[3]	0.097 ± 0.014	
^{10}B 5.92,6.02,6.12 MeV[4]	0.140 ± 0.021	
^{10}B 6.56,6.87, 7.00,7.43 MeV[5]	0.089 ± 0.013	
^{12}C 7.65 MeV	0.0029 ± 0.0004	
^{12}C 9.64 MeV	0.014 ± 0.002	
total	1.00 ± 0.30	
Particle	Multiplicity	Fraction
α	1.47 ± 0.41	0.49 ± 0.14
p	0.24 ± 0.19	0.24 ± 0.19
^{6}Li	0.40 ± 0.07	0.40 ± 0.07

G. Multiplicities of sequentially emitted fragments

The multiplicities of the intermediates obtained from fitting the correlation functions are listed in Tables VI–XII. Apart from those intermediates which were associated with features discussed in the previous section, limits were also obtained for decay from the next higher excited states in most cases. However, limits were not obtained for all possible intermediates (we are especially not sensitive to intermediates which decay by neutron emission) and therefore the total multiplicities must be considered as lower limits.

For all examined exit channels, there are approximately one or more intermediate states per event. Therefore, sequential decay is an important contribution to the fragmentation of the PLF. The multiplicity and fraction of each particle type which originate from the decay of intermediates are also listed in the tables. Sequential decay is very important for the production of alpha particles and lithium fragments. Approximately half, or more, of these particles is produced by sequential decays. For hydrogen isotopes and ^{3}He fragments the fractions are $\gtrsim 30\%$ and $\gtrsim 15\%$, respectively. For the protons, ^{3}He, and tritons, it would be difficult to explain the measured Coulomb shifts if the actual values were significantly larger than these lower limits.

The time scales associated with the decay of these unstable states range from $\hbar/\Gamma = 1.3\times10^{-21}$ for ^{5}Li(g.s.) and ^{8}Be(3.04 MeV) to 9.7×10^{-17} s for ^{8}Be(g.s.) decay. Even for the shortest-lived states, the experimental upper limit of 1.6×10^{-22} s obtained from the Coulomb shifts for the average PLF lifetime is a factor of almost 10 smaller than $\hbar/\Gamma$.

TABLE XIII. Radii of the breakup volume obtained from fitting the correlations functions.

Channel	r_b (fm)
5α	8.5 ± 1.5
$4\alpha+2p$	11 ± 2
$4\alpha+p+d$	12 ± 2
$4\alpha+{}^3$He	11 ± 2
$3\alpha+{}^7$Li$+p$	12 ± 2
$3\alpha+{}^6$Li$+p$	10 ± 2
$4\alpha+p+t$	10 ± 2

Yet, even in these cases, the decay of the intermediate may occur in regions where the target's Coulomb field is not negligible.

H. Radius of breakup volume

The radii r_b of the breakup volumes extracted from fitting the correlation functions are listed in Table XIII. They are all ~ 10 fm and show little dependence on the exit channel, with the possible exception of a somewhat smaller value for the 5α channel. In any case, these values are large compared to the radius of a cold ^{20}Ne ($r=1.4\times A^{1/3}$ fm$=3.8$ fm). However, it is not clear what values of r_b are resonable. Coulomb distortions (holes and overshoots) to the correlation functions are sensitive to both the spacial and temporal dimensions of the fragments' source. In the simulations, only the spacial dimensions were nonzero. If the initial "prompt" decay of the projectile occurred over a short time interval, then this will reduce the magnitude of the Coulomb distortions. Thus the spatial dimensions of the source of projectile fragments can be less than the extracted r_b values. However, the temporal dimensions cannot be too large, given the magnitude of the Coulomb shifts extracted in Sec. IV B.

Even if the temporal dimensions are zero, it does not seem reasonable to expect r_b values close to the radius of a ^{20}Ne. If the emitted particles are packed within a radius of 4 fm, then they will experience nuclear as well as Coulomb interactions. For instance, the interactions between alpha particles do not become Coulomblike until they are separated by at least 6 fm [36]. Thus, a larger effective breakup radius will be needed if only Coulomb interactions are assumed. To include both nuclear and Coulomb interactions, a more refined quantal treatment should be performed to allow for symmetrization effects and resonant interactions.

I. Influence of the target

Up until now, the effect of interactions of the projectile fragments with the target nucleus has been ignored in the discussion of the correlation functions. Such effects have been reported in Refs. [23,37] for two-body correlation functions where the two particles have different Z/A values and hence different Coulomb accelerations in the field of the target nucleus. The effects can be highlighted when the orientation of the relative momentum vector $\mathbf{\Delta p}$ is considered. Let the angle between $\mathbf{\Delta p}$ and the PLF velocity vector be β. For $\beta<90°$, let the lighter particle have a larger longitudinal velocity than the heavier particle. Correlation functions gated on β were obtained for the $\Sigma Z=8$ exit channel $3\alpha+p+d$. This channel was chosen for its large yield in order to reduce the statistical errors. The results obtained for both targets with $\beta<45°$ and $\beta>135°$ are indicated by the solid and open data points, respectively, in Fig. 22. Both the p-α and the p-2α correlation functions show dependences on β. On the other hand the d-α correlations are identical (within statistical errors) for both β gates and both targets. This is not surprising as both the deuteron and the alpha particle have the same Z/A value and in any case the large peak in the correlation function is associated with the ^{6}Li(2.19 MeV) state, which is long lived and hence decays well away from the target's Coulomb field. For the other two correlation functions, the particles have different Z/A values. Results for p-d correlations are not shown, but no large β dependence is observed. However, because of the smaller number of p-d pairs, the statistical errors are larger.

The decay of the short-lived ^{5}Li ground state ($\Gamma=1.5$ MeV) may be responsible for the β dependence for the p-α correlation function at $\Delta p\sim 40$ MeV/c. If the proton from the decay of this state is emitted away from the target ($\beta<45°$), then its larger Coulomb acceleration from the target nucleus will increase the p-α relative momentum. On the other hand, backward emission ($\beta>135°$) will result in a decreased relative momentum. The net result is a shift in the ^{5}Li peak down to smaller Δp values as β becomes larger [23,37].

The features associated with the lower Δp values in the p-α and the p-2α correlation functions were ascribed to ^{9}B(g.s.) and ^{10}B decay for the $\Sigma Z=10$ exit channels. The ^{9}B(g.s.) state is long lived and should not contribute to the observed β dependence. Therefore, the results suggest that a short-lived ^{10}B state is contributing, possibly consistent with the wide 8.07 MeV ($\Gamma=0.8$ MeV) state used in the simulations.

The β dependence of the simulated p-α correlation function is shown in Fig. 23 for $r_b=10$ fm and $z_b=9.6$ fm. For comparison with the experimental results, the solid curve ($\beta<45°$) should be compared with the solid data points and the dotted curve ($\beta>135°$) with the open data points. The simulated β dependence is in the right direction, but its magnitude is too small. Reducing the target-projectile breakup separation (by decreasing z_b) will increase the magnitude of the effect, but because of the large size of the breakup volume, any significant reduction results in an overlap of the target nucleus with this volume. So either the ^{5}Li and ^{10}Be fragments are created preferentially closer to the target than the other particles, or the simulation is inadequate. One possibility is that the presence of the target nucleus affects the whole decay processes and thus the treatment of ^{5}Li decay is inadequate. For instance the Coulomb barrier for proton emission will be lower for small β values, resulting in a larger probability for such emissions. In any case the experimental results indicate that most of these ^{5}Li and ^{10}B fragments are decaying close to the target nucleus.

VI. SEQUENTIAL DECAY

The presence of the unstable intermediates, as indicated by the correlation functions, shows the importance of a sequential decay component of the disassembly process. However, several studies of highly fragmented projectile exit

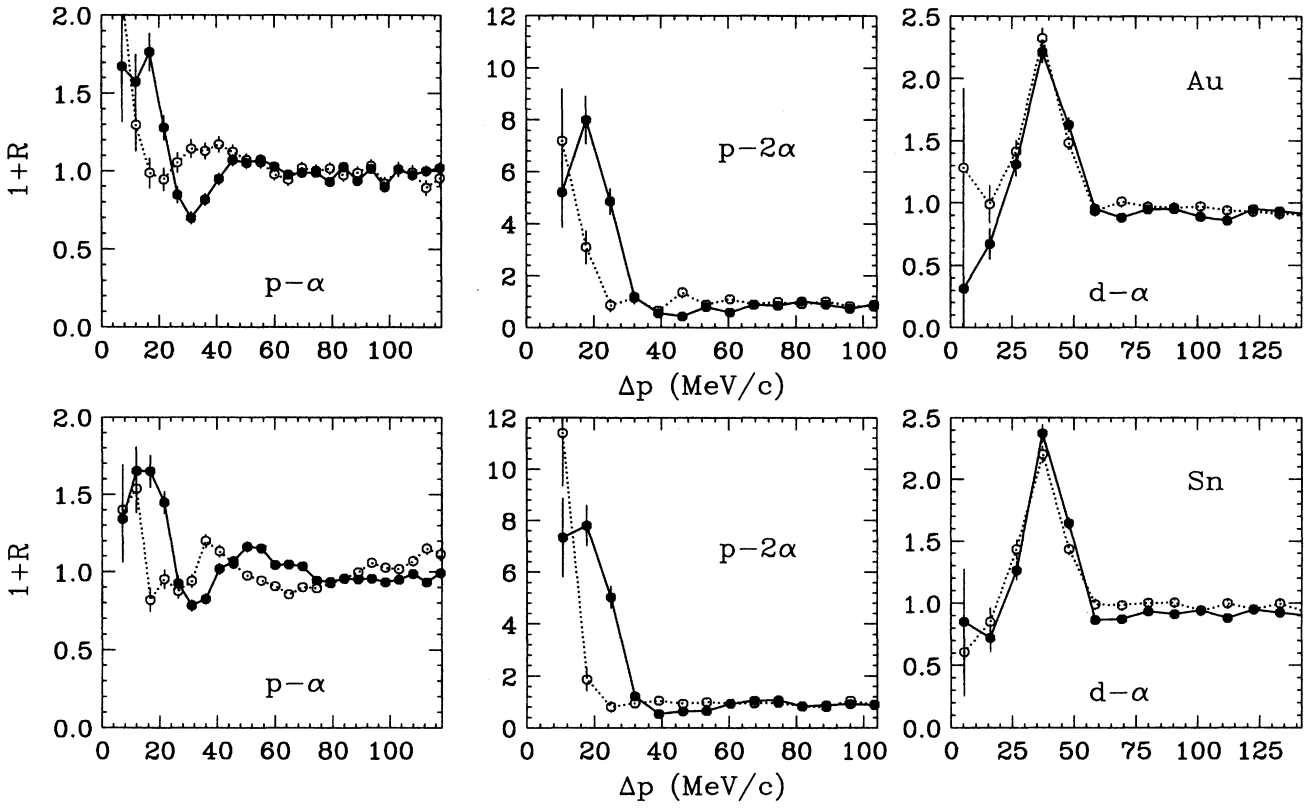

FIG. 22. Experimental correlation functions obtained for the $3\alpha+p+d$ exit channel for two gates on the orientation of the relative momentum vector (β). Solid and open data points were obtained for $\beta<45°$ and $\beta>135°$, respectively. For clarity, the data points are connected by curves. The results for the upper and lower panels were obtained with the Au and Sn targets, respectively.

channels have argued that the whole disassembly process is sequential [4,8,9]. Evidence against this scenario has already been presented in the analysis of the Coulomb shifts in Sec. IV. In this section, the extent to which the experimental correlation functions are consistent with a sequential decay scenario will be examined. The evaporative sequential decay (semiclassical) algorithm of Ref. [11] was incorporated into the Monte Carlo simulations for modeling the 5α exit channel. No interactions between alpha particles emitted in the different decay steps were included. The algorithm was modified to include experimental states in ^{12}C as well as ^{8}Be states. Otherwise, backshifted Fermi gas level densities [38] were assumed for the intermediate systems. For ^{12}C, the backshifted Fermi gas level densities were matched to the density of experimentally known levels at 18 MeV of excitation energy. Events generated by this algorithm were passed through the detector filter. The resulting average 2α probability (29%) was in good agreement with the experimental value (28%), although at high $E_{\rm tot}$ values the predicted probability is too small.

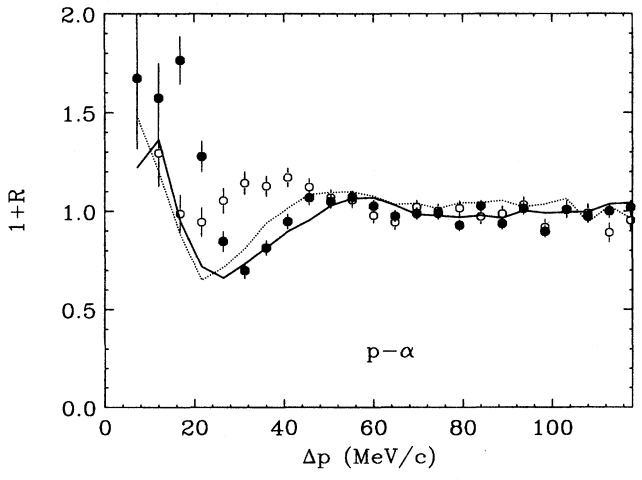

FIG. 23. Experimental (data points) and simulated (curves) correlation functions obtained for the $3\alpha+p+d$ exit channel with the Au target. The solid curves and data points are for $\beta<45°$ while the open data points and dotted curve are for $\beta>135°$.

Before presenting correlation functions, the distributions of relative angles (in the PLF frame) between detected alpha particles will be discussed. To be consistent with other studies, events where a 2α fragment was detected were discarded. The experimental distribution is presented as data points in Figs. 24(a) and 24(b). The distribution has a shoulder for relative angles less than 40° due to alpha particles from the decay of ^{8}Be(g.s.) which are detected in separate detectors. This feature is more pronounced in this work compared to other experimental relative angle distributions

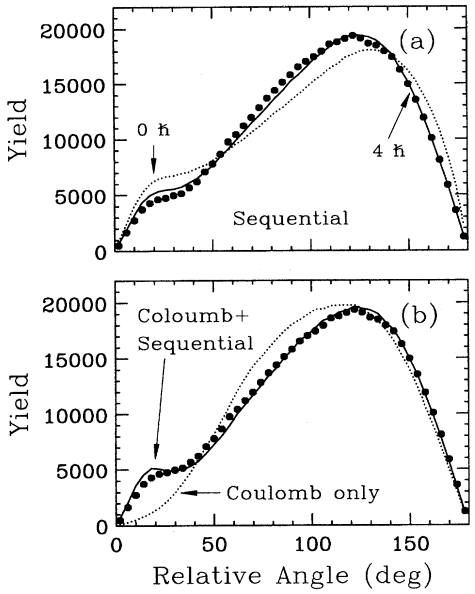

FIG. 24. Distributions of relative angles between the alpha particles in the 5α exit channel. The experimental distribution (data points) is compared in (a) to predictions from the sequential simulations obtained with initial PLF spin values of $0\hbar$ and $4\hbar$. In (b), the experimental distribution is compared with the results of the prompt-plus-sequential simulations (solid curve) used to fit the correlations functions. In contrast, the predictions of a prompt simulation with only Coulomb interactions and no sequential decay are indicated by the dotted curve.

[4,8,9,11] due to the finer granularity of the MINIWALL array.

The distributions obtained with the sequential simulations (curves) are compared to the experimental results in Fig. 24(a). The shape of the simulated sequential distribution depends on the assumed spin J of the PLF [11]. The simulated sequential distributions are consistent with the experimental distribution if $J \geq 4\hbar$ (the sensitivity of the distributions to J is lost for large spins [11]). The predictions of the prompt-plus-sequential simulation of Sec. V, which fit the correlations functions, are shown in Fig. 24(b). It can be seen that this simulation also reproduces the experimental relative angle distributions quite well. In contrast, the prediction of the prompt simulation, without the unstable states, is indicated by the dotted curve. Clearly, in agreement with the conclusions of Refs. [4,8,9], such a prompt simulation, with only Coulomb interactions, is inconsistent with the data. However, as shown above, if unstable states are formed in the prompt decay step, the results are consistent with the experimental relative angle distributions.

Correlations obtained from the sequential decay simulations for $J=4\hbar$ are compared to their experimental counterparts in Fig. 25. Because the sequential algorithm models the decay of an equilibrated system, the predicted longitudinal velocity spectra do not exhibit the low velocity tails. Therefore, in constructing the correlation functions, the sequential velocity distributions were fit using the simulations of Appendix A in order to construct the $\sigma_1(\mathbf{p}_1)\sigma_1(\mathbf{p}_2)$ quantity of Eq. (3).

Structures associated with the 3.04 MeV (arrow 2) states of ^{8}Be and with the 7.65 (arrow 3) and 9.64 MeV (arrow 4) states of ^{12}C are apparent in the simulated correlation functions. The peak for the 7.65 MeV state of ^{12}C is particularly prominent. However, in the experimental correlation function, this structure is significantly less pronounced. The peak in the simulated α-α correlation function at $\Delta p \sim 35$ MeV/c is again associated with the decay of the 7.65 MeV state of ^{12}C. This peak is also not seen in the experimental data. In the α-2α and α-α-α correlation functions, the 7.65 MeV ^{12}C peak is sitting upon a region of reduced correlation. This reduction may be confused with a Coulomb hole feature predicted in the prompt decay simulations. However, no structures resembling the Coulomb overshoot feature (Sec. V) are predicted in the sequential simulations even when other PLF spins and different level densities are assumed. These overshoot features were essential for reproducing the details of all the experimental 5α correlation functions in Sec. V A.

Hence the decay of the PLF by sequential evaporation of alpha particles can be discounted as this scenario significantly overpredicts the yield of the 7.65 MeV ^{12}C state and cannot reproduce the features in the correlation functions due to the Coulomb interactions between all the particles. A sequential decay scenario which commences with a more fissionlike channel (^{8}Be-^{12}C) has not been considered. However, for the $^{16}\mathrm{O} \rightarrow 4\alpha$ decay, a similar fission scenario was discounted [11].

VII. DISCUSSION AND CONCLUSIONS

The analyses of the experimental correlation functions and the Coulomb shift data indicate that there is a range of time scales associated with the fragmentation of the projectile. The following would be a consistent picture of the disassembly process. Because of its interaction with the target, the projectile rapidly disintegrates into a collection of stable and unstable fragments while it is still in contact with target or soon thereafter. Some of these unstable fragments are short lived and decay in a region of space where the target's Coulomb field is still appreciable. Other long-lived fragments decay well away from the target.

In contrast to the above scenario, other studies of highly fragmentated projectile exit channels have concluded that the decay is not prompt, but is completely explained by a series of sequential statistical decays [4,8,9]. These conclusions were obtained from a comparison of the experimental distributions of event shapes and relative angles with simulated prompt and sequential distributions. The simulation of the prompt decay was much like that used in the fitting of the correlation functions in Sec. V, only no unstable intermediates were included. Such a prompt model is also excluded in this work as, without the unstable intermediates, a large number of the features of the correlation functions could not be reproduced.

It has been shown for a representative exit channel that even though sequential decay (only) simulations can reproduce the relative angle distributions, they do not reproduce the correlation functions. Correlation functions and Coulomb shift measurements are therefore more discriminating probes for determining the mechanisms associated the projectile disassembly.

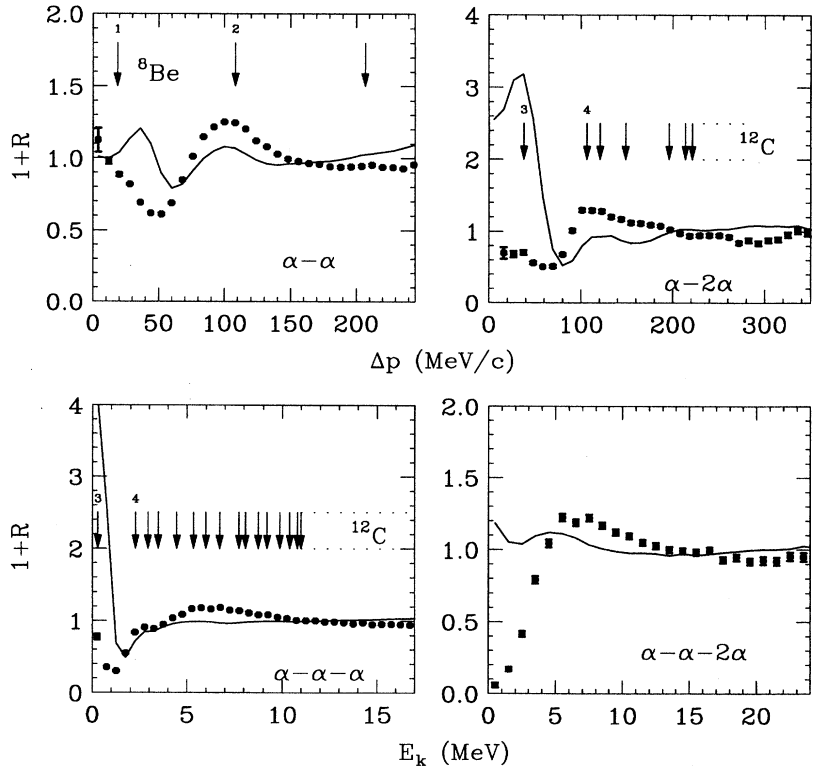

FIG. 25. Correlation function for the 5α exit channel as in Fig. 13, but now the curves show the results for the sequential decay simulation.

Both in the analyses of the Coulomb shifts and the correlation functions, classical mechanics was assumed. To what extent a proper quantum mechanical treatment would modify our conclusions is not known. A classical interpretation of Coulomb shifts measured for the breakup of ^{11}Li [15] has been criticized by Bertsch and Bertulani [39]. In a quantum mechanical model where the target's Coulomb field both excites the projectile and accelerates the fragments, they find that the Coulomb shifts preserve a strong memory of the prebreakup phase. What relevance this calculation has to the present work is not clear, as more localized processes such as nuclear excitation and particle transfers are expected to generate the excitation energy of projectile.

A quantum mechanical treatment of the interactions between the fragments will generate unstable intermediates due to resonant final state interactions. Presumably the alpha particle structure of ^{20}Ne is also important in determining which intermediates are observed.

In conclusion, highly fragmented exit channels of E/A =40 MeV ^{20}Ne projectiles excited through interactions with ^{197}Au and ^{120}Sn target nuclei have been studied. The longitudinal velocity spectra for p, d, t, ^{3}He, α, ^{6}He, ^{6}Li, and ^{7}Li projectile fragments were measured with a 128-element forward array. These velocity spectra were found to be shifted with respect to each other. From differences in the shifts measured with the two targets, contributions from post-breakup accelerations by the target's Coulomb field were extracted. The magnitudes of these shifts indicate that the projectile broke up while still in contact, or near contact, with the target. This time scale is much shorter than that expected for a purely statistical-sequential decay of the projectile. Residual shifts left after subtracting the Coulomb components indicate that not all fragments were emitted from a fully equilibrated projectile, again supporting the conclusion of a fast fragmentation process.

On the other hand, experimental correlation functions indicate that a significant fraction of the fragments is produced by the sequential decay of short- and long-lived unstable intermediates. Therefore very short (prompt) and longer (sequential) time scales are involved in the decay process. A picture emerges of an initial prompt breakup step creating both stable and unstable particles with the unstable particles decaying over a wide variety of time scales.

ACKNOWLEDGMENTS

This work was supported by the U.S. Department of Energy under Contracts Nos. DE-FG02-87-ER40316 and DE-FG02-88-ER40406 and by the National Science Foundation under Grant No. PHY-9214992.

APPENDIX A: MONTE CARLO SIMULATIONS

In order to determine the magnitude of experimental shifts which can be attributed to the detector bias and for construction of correlation functions, the longitudinal and transverse velocity spectra of the fragments were fit. As a starting point, the microcanonical event generating algorithm [33,40], for zero total momentum, was initially used.

(1) Particle momenta are initially chosen from a canonical distribution with some arbitrary temperature.

(2) A constant momentum vector is than subtracted from each particle momentum in order to make the total momentum zero.

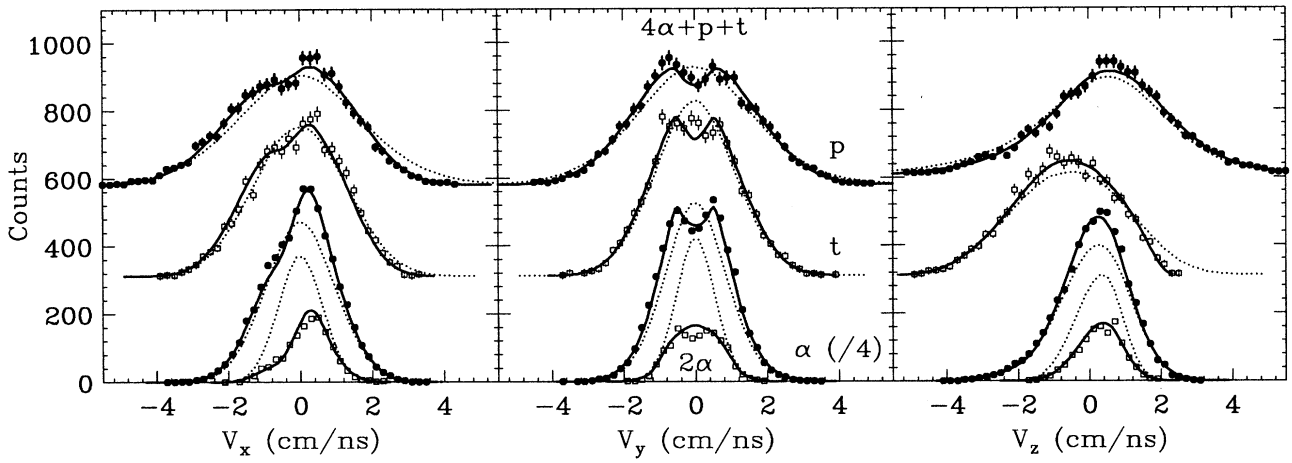

FIG. 26. Experimental transverse (x,y) and longitudinal (z) velocity spectra obtained for the $4\alpha+p+t$ exit channel with the Sn target. For clarity, the spectra have been shifted vertically and scaled as indicated in the parentheses. Fits to these spectra are indicated by the solid curves and the primary distributions used in the simulation are indicated by the dotted curves.

(3) The momentum vectors are then scaled so as to reproduce the desired total kinetic energy of the fragments, $E_{\rm tot}$.

Events generated with this algorithm were (Lorentz) transformed to the frame of the PLF, and the simulated fragments were then passed through the MINIWALL filter. The same event selection criteria were then applied as per the experimental data. The primary projectile velocity $E_{\rm tot}$ and angular distributions were obtained by an iterative approach [11] so that secondary distributions reproduced the experimental results. To reproduce the experimental 2α probability, a fraction of the events were generated with one or two ^{8}Be(g.s.) fragments. These fragments were assumed to decay isotropically. If two alpha particles entered the same detector, they were treated as a 2α fragment no matter whether they originated from a ^{8}Be fragment or not. The experimental probability per event of detecting one or two 2α fragments in the 5α exit channel is shown as a function of $E_{\rm tot}$ in Fig. 4 by the data points. The solid curves indicate the ^{8}Be(g.s.) probability per event needed to reproduce the experimental results.

The above microcanonical simulation reproduces some of the general trends of the particle velocity spectra. However, it does not reproduce the magnitude of the shifts and the low velocity tails of the longitudinal velocity spectra. Also the widths of both the longitudinal and transverse spectra are not correct. To correct these deficiencies, the first step of the above algorithm was modified. A different temperature was chosen for each particle type and direction. A shift was introduced for each particle type in the longitude direction. To produce low velocity tails, a second longitudinal component with the same temperature, lower probability, and shifted down in velocity was also included. An example of the excellent fits obtained with this modified algorithm is shown in Fig. 26 for the $4\alpha+p+t$ exit channel with the Sn target. The fitting parameters are not listed as there are a large number of them and it is not clear that they have any physical significance. Note that generally the temperature in the out-of-plane direction (y) is a little smaller than the in-plane values. This could be a consequence of an aligned projectile spin which would suppress emissions in the out-of-plane direction. The second longitudinal component was used with $\sim$5% probability; however, it is not clear whether this represents a second component in reality.

The primary velocity distributions (before the detector response is added) are indicated by the dotted curves in Fig. 26. For the 2α fragments, the dotted curve shown is for the ^{8}Be(g.s.) fragments. The difference in yield between it and the experiment 2α spectra reflects the probability that a ^{8}Be fragment gets detected as a 2α particle. The transverse velocity spectra are strongly distorted at $V_{x,y}\sim 0$ by the MINIWALL angular acceptance (fragments with small transverse velocities generally pass through the hole in the MINIWALL at $\theta_{\rm lab}<3.4°$ and are not detected). However, these distortions are well reproduced in the simulations. The longitudinal velocity spectra for tritons is distorted at large velocities as high energy tritons punch through the detectors. A small shift can be seen between the simulated primary and secondary longitudinal spectra for protons.

Small shifts between the average primary and secondary velocities were found for protons, tritons, and ^{3}He fragments. Protons and ^{3}He fragments are shifted up in velocity, while tritons were shifted down. These shifts are a result of the low energy threshold for ^{3}He fragments and the punch-through energy for tritons. For protons, the cause of the shift is the lack of acceptance for $\theta_{\rm lab}<25.5°$. Protons can only arrive at such large laboratory angles if they are emitted sideways and slightly backwards from the projectile. These results were used to obtain the corrected shifts in Fig. 9. The errors on the correction factors are associated with the range of values obtained by varying the fitting parameters such that reasonable fits to the spectra were still obtained. Spectra obtained for two targets have almost identical correction factors if the same fitting parameters were used [except for the longitudinal shift introduced in step (1)].

APPENDIX B: REACTIONS IN DETECTOR

As the energy increases and range of a particle becomes longer, the probability that the particle will undergo a nuclear

reaction in the detector material can be important. Such reactions can result in a depletion in the number of identified high energy particles, thereby shifting the average velocity of these particles. The magnitude of this depletion and the extent to which it may be confused with a shift due to the post-breakup target acceleration effect are investigated in this appendix.

For a beam of N particles of energy E at some point in the detector material, the differential equation governing the loss of these particles due to nuclear reactions is

$$dN/dE = -\frac{n\sigma(E)N}{dE/dx}, \tag{B1}$$

where σ is the reaction cross section, dE/dx is the stopping power, and n is the number of detector nuclei per unit volume. The total fractional loss over the range of the particle can be determined by integration of this equation. The stopping power of particles in CsI was estimated from Ref. [41]. Reaction cross sections were estimated from optical-model calculations. The optical-model parameters were taken from the compilation of Ref. [42], selecting the values for the most similar reaction at the highest energy available. The cross sections approach geometric limits at the highest energies and so the energy dependence is not important. The dependence of the fractional particle loss as a function of energy per nucleon is displayed in Fig. 27 for the hydrogen and helium isotopes. The results for lithium isotopes are very similar to that for alpha particles. At any given value of E/A, tritons have the largest fractional loss. This is primarily due to their longer range. For $E/A = 40$ MeV, the fractional loss is 10% for tritons compared to 2% for protons.

To investigate the effect of this particle loss on the velocity spectra of the projectile fragments, the reaction probabilities were incorporated into the Monte Carlo simulations in Appendix A and Sec. V. If a reaction in a detector was simulated, then the whole event was excluded for the subsequent analysis. The fractional loss shifts down the average velocities of all fragments, but only slightly. For determining the magnitude of Coulomb shifts, the important quantity is the relative shifts. It was found that these are small compared to those produced by the detector thresholds and angular acceptance of the MINIWALL detectors. The largest consequence of the fractional loss was to reduce the efficiency for detecting all fragments in a channel.

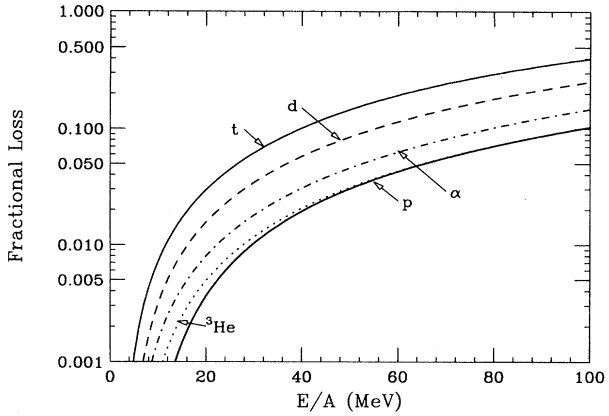

FIG. 27. Predicted fractional loss of a particle type due to nuclear reactions of the particles with the CsI material of the detectors. The fractional loss is plotted as a function of the energy per nucleon of the particle.

[1] J.R. Wu, C.C. Chang, and D.H. Holmgren, Phys. Rev. Lett. **40**, 1013 (1978).
[2] A.C. Schotter, A.N. Bice, J.M. Wouters, W.D. Rae, and J. Cerny, Phys. Rev. Lett. **46**, 12 (1981).
[3] B.G. Harvey, Phys. Lett. B **252**, 536 (1990).
[4] B.A. Harmon, J. Pouliot, J.A. López, J. Suro, R. Knop, Y. Chan, D.E. DiGregorio, and R.G. Stokstad, Phys. Lett. B **235**, 234 (1990).
[5] J. Pouliot, Y. Chan, A. Decal, D.E. DiGregorio, B.A. Harman, R. Knop, M.E. Ortiz, E. Plagnol, R.G. Stokstad, C. Moisan, L. Potvin, C. Rioux, and R. Roy, Phys. Lett. B **223**, 16 (1989).
[6] R. Laforest, D. Doré, J. Pouliot, R. Roy, C. St-Pierre, G. Auger, P. Bricault, S. Groult, E. Plagnol, and D. Horn, Nucl. Phys. **A568**, 350 (1994).
[7] D. Doré, L. Beaulieu, R. Laforest, J.L. Laville, O. Lopez, J. Pouliot, R. Régimbart, R. Roy, J.C. Steckmeyer, and C. St-Pierre, Phys. Lett. B **323**, 103 (1994).
[8] J. Pouliot, D. Doré, R. Laforest, R. Roy, C. St-Pierre, and J.A. Lopez, Phys. Lett. B **299**, 210 (1993).
[9] A. Badalà, R. Barbera, A. Palmeri, G.S. Pappalardo, and F. Riggi, Phys. Rev. C **48**, 633 (1993).
[10] L.G. Moretto and G.J. Wozniak, Annu. Rev. Nucl. Part. Sci. **43**, 379 (1993).
[11] R.J. Charity, J. Barreto, L.G. Sobotka, D.G. Sarantites, D.W. Stracener, A. Chbihi, N.G. Nicolis, R. Auble, C. Baktash, J.R. Beene, F. Bertrand, M. Halbert, D.C. Hensley, D.J. Horen, C. Ludemann, M. Thoennessen, and R. Varner, Phys. Rev. C **46**, 1951 (1992).
[12] D.H. Boal, C.K. Gelbke, and B.K. Jennings, Rev. Mod. Phys. **62**, 553 (1990).
[13] W. Bauer, C.K. Gelbke, and S. Pratt, Annu. Rev. Nucl. Part. Sci. **42**, 77 (1992).
[14] M. Murphy, S. Gil, M.N. Harakeh, A. Ray, A.G. Seamster, R. Vandenbosch, and T.C. Awes, Phys. Rev. Lett. **53**, 1543 (1984).
[15] D. Sacket, K. Ieki, A. Galonsky, C.A. Bertulani, H. Esbensen, J.J. Kruse, W.G. Lynch, D.J. Morrissey, N.A. Orr, B.M. Sherrill, H. Schulz, A. Sustich, J.A. Winger, F. Deák, Á. Horváth, Á. Kiss, Z. Seres, J.J. Kolata, R.E. Warner, and D.L. Humphrey, Phys. Rev. C **48**, 118 (1993); Phys. Rev. Lett. **70**, 730 (1993).
[16] R.J. Charity, L.G. Sobotka, G. Van Buren, F.A. Tibbals, J. Barreto, D.R. Bowman, M. Chartier, J. Dinius, D. Fox, C.K. Gelbke, D.O. Handzy, W.C. Hsi, P.F. Hua, A.S. Kirov, M.A. Lisa, W.G. Lynch, G.F. Peaslee, L. Phair, D.G. Sarantites, C.

Schwarz, R.T. de Souza, M.B. Tsang, and C. Williams, Phys. Lett. B **323**, 113 (1994).
[17] D.W. Stracener, D.G. Sarantites, L.G. Sobotka, J. Elson, J.T. Hood, Z. Majka, V. Abenante, A. Chbihi, and D.C. Hensley, Nucl. Instrum. Methods A **294**, 485 (1990).
[18] B.M. Sherril, D.J. Morrissey, J.A. Nolan, Jr., N. Orr, and J.A. Winger, Nucl. Instrum. Methods B **70**, 298 (1992).
[19] R.T. de Souza, N. Carlin, Y.D. Kim, J. Ottarson, L. Phair, D.R. Bowman, C.K. Gelbke, W.G. Gong, W.G. Lynch, R.A. Pelak, T. Peterson, G. Poggi, M.B. Tsang, and H.M. Xu, Nucl. Instrum. Methods A **295**, 109 (1990).
[20] T. Ericson and T. Mayer-Kuckuk, Annu. Rev. Nucl. Sci. **16**, 183 (1966).
[21] W.D. Myers, *Droplet Model of Atomic Nuclei* (IFI/Plenum, New York, 1977).
[22] O. Schapiro, A.R. DeAngelis, and D.H.E. Gross, Nucl. Phys. **A568**, 333 (1994).
[23] J. Pochodzalla, C.K. Gelbke, W.G. Lynch, M. Maier, D. Ardouin, H. Delangrange, H. Doubre, C. Grégoire, A. Kyanowski, W. Mittig, A. Péhaire, J. Péter, F. Saint-Laurent, B. Zwieglinski, G. Bizard, F. Lefébvres, B. Tamain, J. Québert, Y.P. Viyogi, W.A. Friedman, and D.H. Boal, Phys. Rev. C **35**, 1695 (1987).
[24] S.E. Koonin, Phys. Lett. **70B**, 43 (1977).
[25] S. Pratt and M.B. Tsang, Phys. Rev. C **36**, 2390 (1987).
[26] W.G. Gong, W. Bauer, C.K. Gelbke, and S. Pratt, Phys. Rev. C **43**, 781 (1991).
[27] F. Ajzenberg-Selove, Nucl. Phys. **A490**, 1 (1988).
[28] F. Ajzenberg-Selove, Nucl. Phys. **A506**, 1 (1990).
[29] C. M. Jones, G. C. Phillips, and P. D. Miller, Phys. Rev. **117**, 525 (1960).
[30] Th. Stammbach and R.L. Walters, Nucl. Phys. **A180**, 225 (1960).
[31] C. Werntz, Phys. Rev. **133**, B19 (1964).
[32] A.M. Lane and R.G. Thomas, Rev. Mod. Phys. **30**, 257 (1958).
[33] J. Randrup, Comput. Phys. Commun. **59**, 439 (1990).
[34] H.H. Hackenbroich, T.H. Seligman, W. Zahn, and D. Fick, Phys. Lett. B **62**, 121 (1976).
[35] R. Čaplar, H. Gemmeke, L. Lassen, W. Weiss, and D. Fick, Nucl. Phys. **A342**, 71 (1980).
[36] B. Buck, H. Friedrich, and C. Wheatley, Nucl. Phys. **A275**, 246 (1977).
[37] J. Pochodzalla, W.A. Friedman, C.K. Gelbke, W.G. Lynch, M. Maier, D. Ardouin, H. Delagrange, H. Doubre, C. Grégoire, A. Kyanowski, W. Mittig, A. Péghaire, J. Péter, F. Saint-Laurent, Y.P. Viyogi, B. Zwieglinski, G. Bizard, F. Lefébvres, B. Tamain, and J. Québert, Phys. Lett. **161B**, 256 (1985).
[38] W. Dilig, W. Schantl, H. Vonach, and M. Uhl, Nucl. Phys. **A217**, 269 (1973).
[39] G.F. Bertsch and C.A. Bertulani, Nucl. Phys. **A556**, 136 (1993); Phys. Rev. C **49**, 2839 (1994).
[40] T.C. Awes and C.K. Gelbke, Phys. Rev. C **27**, 137 (1983).
[41] J.F. Ziegler, J.P. Biersack, and U. Littmark, *The Stopping Power and Ranges of Ions in Matter* (Pergamon, London, 1985), Vols. 1 and 2.
[42] C.M. Pery and F.G. Pery, At. Data Nucl. Data Tables **17**, 1 (1976).